Monthly Notices
of the
ROYAL ASTRONOMICAL SOCIETY

MNRAS **509,** 1587–1604 (2022)
Advance Access publication 2021 October 20

https://doi.org/10.1093/mnras/stab3001

A multimission catalogue of ultraluminous X-ray source candidates

D. J. Walton [1,2★] A. D. A. Mackenzie,[3] H. Gully,[4] N. R. Patel,[5] T. P. Roberts,[3] H. P. Earnshaw [6] and S. Mateos[7]

[1]*Institute of Astronomy, University of Cambridge, Madingley Road, Cambridge CB3 0HA, UK*
[2]*Centre for Astrophysics Research, University of Hertfordshire, College Lane, Hatfield AL10 9AB, UK*
[3]*Centre for Extragalactic Astronomy, Department of Physics, Durham University, South Road, Durham DH1 3LE, UK*
[4]*School of Physics, Astronomy, University of Nottingham, University Park, Nottingham NG7 2RD, UK*
[5]*Department of Physics and Astronomy, Pevensey Building, University of Sussex, Brighton BN1 9QH, UK*
[6]*Cahill Center for Astronomy and Astrophysics, California Institute of Technology, Pasadena, CA 91125, USA*
[7]*Instituto de Física de Cantabria (CSIC-UC), Avenida de los Castros, E-39005 Santander, Spain*

Accepted 2021 October 14. Received 2021 October 8; in original form 2021 September 1

ABSTRACT

We present a new, multimission catalogue of ultraluminous X-ray source (ULX) candidates, based on recent data releases from each of the *XMM–Newton*, *Swift*, and *Chandra* observatories (the 4XMM-DR10, 2SXPS, and CSC2 catalogues, respectively). This has been compiled by cross-correlating each of these X-ray archives with a large sample of galaxies primarily drawn from the HyperLEDA archive. Significant efforts have been made to clean the sample of known non-ULX contaminants (e.g. foreground stars, background active galactic nuclei, supernovae), and also to identify ULX candidates that are common to the different X-ray catalogues utilized, allowing us to produce a combined 'master' list of unique sources. Our sample contains 1843 ULX candidates associated with 951 different host galaxies, making it the largest ULX catalogue compiled to date. Of these, 689 sources are catalogued as ULX candidates for the first time. Our primary motivation is to identify new sources of interest for detailed follow-up studies, and within our catalogue we have already found one new extreme ULX candidate that has high S/N data in the archive: NGC 3044 ULX1. This source has a peak luminosity of $L_{\rm X,peak} \sim 10^{40}$ erg s^{-1}, and the *XMM–Newton* spectrum of the source while at this peak flux is very similar to other, better-studied extreme ULXs that are now understood to be local examples of super-Eddington accretion. This likely indicates that NGC 3044 ULX1 is another source accreting at super-Eddington rates. We expect that this catalogue will be a valuable resource for planning future observations of ULXs – both with our current and future X-ray facilities – to further improve our understanding of this enigmatic population.

Key words: X-rays: binaries – X-rays: individual: NGC 3044 ULX1.

1 INTRODUCTION

Our understanding of ultraluminous X-ray sources (ULXs) – off-nuclear X-ray sources with luminosities in excess of 10^{39} erg s^{-1} – has evolved significantly over the past few years. Historically, the debate regarding the nature of these sources has focused on whether they represent a population of sub-Eddington 'intermediate-mass' black holes (IMBHs with $M_{\rm BH} \sim 10^2$–10^5 M$_\odot$; e.g. Colbert & Mushotzky 1999; Miller et al. 2004; Strohmayer & Mushotzky 2009) or a population of super-Eddington but otherwise normal stellar remnants (e.g. King et al. 2001; Poutanen et al. 2007; Middleton et al. 2015); see Kaaret, Feng & Roberts (2017) for a recent review. Although evidence for large black holes is now being seen by LIGO (most notably the recent detection of a BH–BH merger resulting in a ∼150 M$_\odot$ remnant; Abbott et al. 2020), the general consensus is now that the majority of ULXs represent a population of super-Eddington accretors, thanks in particular to the broad-band spectral and timing studies possible in the *NuSTAR* era (Harrison et al. 2013) and the high-resolution spectra provided by *XMM–Newton* (Jansen et al. 2001).

The broad-band spectra obtained early in the *NuSTAR* mission demonstrated that ULX spectra are clearly distinct from standard modes of sub-Eddington accretion (e.g. Bachetti et al. 2013; Walton et al. 2013, 2014, 2015; Mukherjee et al. 2015; Rana et al. 2015), confirming prior indications from *XMM–Newton* (e.g. Stobbart, Roberts & Wilms 2006; Gladstone, Roberts & Done 2009), and instead revealed high-energy spectra consistent with broad expectations for super-Eddington accretion (i.e. spectra that appear to show a strong contribution from hot, luminous accretion discs, e.g. Shakura & Sunyaev 1973; Abramowicz et al. 1988; Poutanen et al. 2007). The super-Eddington nature of at least some ULXs was then spectacularly confirmed with the discovery that the ULX M82 X-2 ($L_{\rm X,peak} \sim 2 \times 10^{40}$ erg s^{-1}) is actually powered by a highly super-Eddington neutron star, following the detection of coherent X-ray pulsations (Bachetti et al. 2014). Five more ULX pulsars have since been discovered (Fürst et al. 2016; Israel et al. 2017a,b; Carpano et al. 2018; Sathyaprakash et al. 2019; Rodríguez Castillo et al. 2020), revealing an accretion regime that extends up to $L/L_{\rm E} \sim 500$. In addition to the broad-band spectra and the discovery of ULX pulsars, we now have evidence in ULX data for the powerful outflows ubiquitously predicted by models of super-Eddington accretion via the detection of blueshifted atomic features.

★ E-mail: dwalton@ast.cam.ac.uk

These have been seen primarily in the low-energy *XMM–Newton* Reflection Grating Spectrometer (RGS) data, but also in the iron *K* band in a couple of cases (Pinto, Middleton & Fabian 2016; Walton et al. 2016; Pinto et al. 2017, 2020; Kosec et al. 2018a,b). These outflows exhibit extreme velocities ($\sim$0.1–0.3c), implying they carry a significant additional energetic output from these already extreme X-ray binary systems.

Nevertheless, important questions still remain regarding the ULX population. Although it is now speculated that ULX pulsars could actually make up a significant fraction of these sources (e.g. Koliopanos et al. 2017; Pintore et al. 2017; Walton et al. 2018b), their exact contribution is still highly uncertain. Is there also a significant population of black hole ULXs, and if so could these be the progenitors of the BH–BH mergers now regularly being seen by LIGO (Inoue, Tanaka & Isobe 2016; Mondal et al. 2020)? Given the history of the field, it is easy to forget that we still do not have a single ULX with a well-constrained mass function that unambiguously requires the accretor to be a black hole. Can black hole ULXs (assuming they exist) reach the same extreme Eddington ratios as ULX pulsars, or is this somehow related to the magnetic nature of these objects (as suggested by Dall'Osso, Perna & Stella 2015; Mushtukov et al. 2015)? What fraction of the total energetic output is radiative, and what fraction is kinetic (i.e. carried by winds/outflows) at these extreme accretion rates? Understanding this last issue may in turn be critical for understanding early-Universe SMBH growth (and associated feedback), given that $\sim10^9$ M$_\odot$ black holes are now being observed when the Universe was only $\sim$0.7 Gyr old (e.g. Bañados et al. 2018).

Furthermore, although the overall population is now expected to be dominated by super-Eddington accretors, there are still rare individual sources among the ULX population that remain good IMBH candidates. Most notable among these is the case of ESO 243–49 HLX1, which reaches an astonishing luminosity of $L_{\rm X,peak} \sim 10^{42}$ erg s^{-1} (Farrell et al. 2009). In contrast to the vast majority of the ULX population, this source does behave as expected for a scaled-up sub-Eddington X-ray binary (Servillat et al. 2011; Webb et al. 2012). Furthermore, M82 X-1 has long been thought of as an IMBH candidate because of its X-ray properties (e.g. Feng & Kaaret 2010; Pasham, Strohmayer & Mushotzky 2014, although see Brightman et al. 2020a for caveats), and NGC 2276–3c has also been suggested as an IMBH candidate owing to its position on the radio–X-ray Fundamental Plane (Mezcua et al. 2015). Identifying further IMBH candidates remains of significant interest, given the scarcity of compelling cases among the ULX population.

Key to advancing all of these areas are efforts to grow the broader ULX population and provide larger samples with which to undertake statistical studies of ULXs and identify notable individual sources for follow-up study. Most previous efforts have focused on searching for ULXs in individual mission archives, using in particular *ROSAT* (Roberts & Warwick 2000; Colbert & Ptak 2002; Liu & Bregman 2005), *Chandra* (Swartz et al. 2004; Liu 2011; Gong, Liu & Maccarone 2016; Kovlakas et al. 2020), and *XMM–Newton* (Walton et al. 2011b; Earnshaw et al. 2019b). Focusing on data from a single mission has the advantage that everything (source selection, energy bands) can be treated in a uniform manner, which is important for performing population-based studies where selection biases need to be carefully controlled. However, this comes at the expense of limiting the sky area/temporal coverage utilized relative to that available in the full, multimission X-ray archive, both of which are key factors in terms of identifying individual sources that may be of particular interest.

Here, we present the results of a search for new ULX candidates, combining data from all of the public archives from the major soft X-ray imaging observatories currently operational: *XMM–Newton* (Jansen et al. 2001), *Chandra* (Weisskopf et al. 2002), and the *Neil Gehrels Swift Observatory* (hereafter *Swift*; Gehrels et al. 2004). In particular, we make use of the 4XMM-DR10, CSC2, and 2SXPS source catalogues (Webb et al. 2020; Evans et al. 2020a,b). Although combining the data from these facilities does formally introduce some non-uniformity to the selection, our primary aim is to compile the largest raw sample of ULX candidates to date, facilitating searches for sources that are bright enough for detailed follow-up with current and future X-ray facilities, as well as searches for sources with multiwavelength counterparts. This is of particular interest with both *XRISM* (XRISM Science Team 2020) and *Athena* (Nandra et al. 2013) on the horizon, as well as the new facilities due to come online at longer wavelengths (e.g. 30-m class optical telescopes, *JWST*, the SKA, etc.).

The paper is structured as follows: in Section 2, we outline the galaxy sample within which we search for ULX candidates, and in Section 3 we discuss our procedure for identifying ULX candidates from the individual archives. Section 4 presents our final, merged sample of ULX candidates, and we highlight the case of NGC 3044 ULX1 – a new extreme ULX discovered here – in Section 5. Finally, we summarize our findings in Section 6.

2 GALAXY SAMPLE

In addition to the various X-ray archives considered here, the other major input required for this work is a catalogue of galaxies within which to search for ULXs. Here, we primarily use the HyperLEDA data base (Makarov et al. 2014), initially selecting everything labelled as a galaxy. We focus on HyperLEDA because this is one of the largest homogenized compilations of known galaxies available in the literature. However, we further supplement these galaxies with the latest version of the Catalogue of Nearby Galaxies (CNG; Karachentsev, Kaisina & Makarov 2018).

For our work here, we need to be able to define the sky area subtended by the galaxy (in order to positionally match X-ray sources) as well as the distance to the galaxy (in order to compute source luminosities). For the galaxy areas, we assume the extent of each galaxy is determined by the elliptical region defined by its D25 isophote (i.e. the best elliptical fit to the area over which *B*-band surface brightness of the galaxy exceeds 25 mag arcsec^{-2}), which is given in HyperLEDA (where this information is available). However, CNG uses the Holmberg radius to define the semimajor axis of the galaxy ellipse instead, which corresponds to a surface brightness of 26.5 mag arcsec^{-2}. For the subset of galaxies included in both HyperLEDA and CNG, we therefore calculate an empirical correction between the D25 semimajor axes ($R_{\rm D25}$) and the Holmberg radii ($R_{\rm Holm}$), and then apply this to any remaining galaxies that are only included in CNG in an attempt to normalize these to the D25 definition. On average, we find $R_{\rm Holm} = (1.26 \pm 0.02)R_{\rm D25}$ (where the uncertainty quoted here is the 1σ standard error on the mean). Although the full set of D25 information (semimajor axis, semiminor axis, position angle) is obviously required to search the full sky area subtended by the galaxy, in cases where the position angle is missing it is still possible to search for ULX candidates within a circular region defined by the semiminor axis, as this will always be within the galaxy area regardless of the orientation of its full elliptical region. We therefore also retain these galaxies in our input sample. However, any galaxies in the HyperLEDA/CNG catalogues that do

not have sufficient information that we can compute at least their D25 semiminor axes are discarded.

For the majority of the galaxies considered, we compute distances based on their measured redshifts (z) assuming they adhere to the Hubble flow. However, where redshift-independent distance estimates are available, we prioritize these measurements. HyperLEDA and CNG both include these based on a variety of different methods (via e.g. Cepheid variables, the tip of the red giant branch, the Tully–Fischer relationship), and we further supplement these with distance measurements from the latest version of the Cosmicflows galaxy catalogue (Tully, Courtois & Sorce 2016). Such measurements are particularly critical for very nearby galaxies (recession velocities $cz < 1000$ km s^{-1}), where peculiar motions can dominate over the Hubble flow. For these galaxies, we therefore also collected further redshift-independent distance from the NASA Extragalactic Database where such measurements were not available in any of the HyperLEDA/CNG/Cosmicflows catalogues. Where there are multiple distance estimates available among these catalogues, we prioritize them in the following order: Cosmicflows > CNG > Hyperleda > NED > Hubble flow, but we stress that in the majority of cases there is generally good agreement between the different catalogues regarding the redshift-independent distance estimates. However, since a reasonably reliable distance estimate is in turn critical for a reliable luminosity calculation, we therefore discard galaxies with recession velocities $cz < 1000$ km s^{-1} where there is no redshift-independent distance estimate available in any of the above (similar to both Walton et al. 2011b and Earnshaw et al. 2019b).

The final galaxy sample utilized here consists of 966 010 entries, after accounting for the requirements outlined above, the vast majority of which come from HyperLEDA (only 215 of these galaxies are found in CNG but not HyperLEDA). Just under half of these galaxies have morphology estimates available in the form of the Hubble type, T. Following Walton et al. (2011b), for these galaxies we make the distinction between spiral galaxies ($T \geq 1$, including irregular galaxies) and elliptical galaxies ($T < 1$, including lenticular galaxies). We show the distance distributions for the full galaxy sample utilized here, as well as some of these subsets, in Fig. 1. The majority of the galaxies considered are within a Gpc, although the galaxies for which morphology information is not available do have larger distances on average than those where the morphology has been identified.

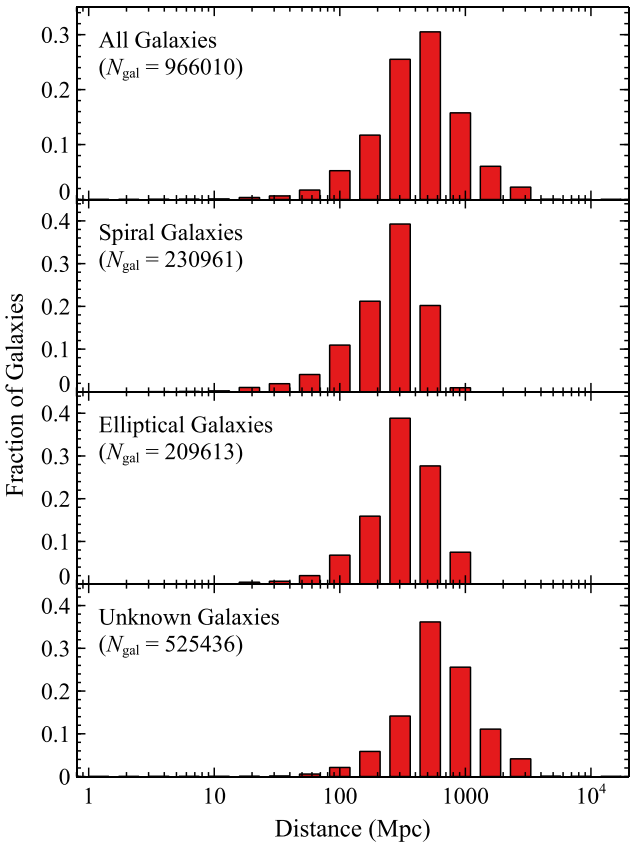

Figure 1. Distance distributions for the full galaxy sample utilized here (top panel), galaxies identified as spiral ($T \geq 1$) and elliptical ($T < 1$) galaxies (upper-middle and lower-middle panels, respectively), and for galaxies where morphology information is not available (bottom panel).

3 SELECTION OF ULX CANDIDATES

3.1 Basic approach

We take the same basic approach to selecting ULXs for each of the three X-ray source catalogues utilized here (4XMM-DR10, 2SXPS, and CSC2). Our initial analysis of these individual archives can be broadly summarized into five main steps, as described below. Many of the specific details differ for the different catalogues utilized, owing to the differences between the different X-ray observatories they are derived from and the different formats in which the data are provided; these details are discussed in Section 3.2.

3.1.1 Step 1 – positional match

First, we perform a positional cross-match between our input galaxy list and each X-ray catalogue; as noted above, for galaxies where the full set of spatial information is available (both the major and minor axes, and the position angle) we perform a standard elliptical match around the position of the galaxy (i.e. utilizing the full sky area it subtends), while for galaxies where the position angle is missing we perform a circular match within the radius set by the semiminor axis (and thus potentially only utilize a fraction of its sky area). Where relevant, only X-ray sources listed as being point-like are retained (both CSC2 and 4XMM-DR10 also contain extended sources, while in principle 2SXPS only includes point sources).

There are inevitably a small subset of X-ray sources that are consistent with being associated with more than one galaxy in our initial matched source lists. In these cases, we make sure to retain only one of the repeat entries in order to avoid individual X-ray sources/detections appearing more than once. To do so, we initially associate the X-ray source with the galaxy for which it is closest to the centre. This is because we expect the majority of these cases to be interacting galaxies, which by definition will be at essentially the same distance, and on average the density of ULXs is known to increase as you approach the galaxy centre (Swartz et al. 2011). However, we re-visit this assumption at the end of our analysis of the individual archives (i.e. after step 5), and assess whether the different galaxy distances really are similar for any remaining sources that are potentially associated with more than one galaxy. Here, we treat galaxies with distances that differ by <15 per cent as having similar distances. Where this is not the case, such that the potential host galaxies appear to be un-associated galaxies that happen to overlap when viewed in projection, we switch the association of the X-ray source to the less distant galaxy. This is both a conservative approach, resulting in lower X-ray luminosities, and also probably a more

realistic assumption in these situations, as the enhanced absorption by gas and dust in the foreground galaxy would mean sources in the background galaxy are less likely to be seen as ULXs based on their observed luminosities. For any sources where the association is changed at this stage, the luminosities are re-evaluated (see step 2), and any sources that no longer meet the ULX criterion are excluded.

3.1.2 Step 2 – luminosity cut

With our positionally matched source lists, we then compute X-ray luminosities using our preferred galaxy distance. Here, we use the full band fluxes available in each of the individual X-ray catalogues (see Section 3.2). These bandpasses are not precisely identical, but are sufficiently similar that we consider this a reasonable compromise for the sake of simplicity, particularly in light of the simple spectral forms assumed when estimating these fluxes (see Section 3.2). Attempting to correct all of the fluxes to have a common treatment is non-trivial, particularly given the time-dependent nature of the *Chandra* instrumental responses (owing to the long-term build-up of the ACIS contamination layer; Plucinsky et al. 2018). With the luminosities in hand, we retain only sources with a full band luminosity that exceeds 10^{39} erg s^{-1}, the standard definition of a ULX. In particular, we select sources that have exhibited luminosities in excess of 10^{39} erg s^{-1} during any individual observation of the source, allowing us to select both persistent and transient/highly variable ULXs. This is a key consideration here, since the latter are now being detected in increasing numbers as our X-ray archives continue to grow (e.g. Middleton et al. 2012, 2013; Soria et al. 2012; Pintore et al. 2018, 2020; Earnshaw et al. 2019a, 2020; van Haaften et al. 2019; Brightman et al. 2020b; Walton et al. 2021), and may be of particular interest in the context of identifying good ULX pulsar candidates (e.g. Tsygankov et al. 2016; Earnshaw, Roberts & Sathyaprakash 2018; Song et al. 2020).

3.1.3 Step 3 – quality flag cut

Each of the X-ray catalogues utilized here contain a variety of information that relate to the robustness of the X-ray detection included and the source properties derived. In each case, we make use of this information to ensure that we only consider sources for which the available X-ray information is reliable, further discarding sources where there are concerns that this may not be the case. The approach taken here is necessarily specific to each of the individual catalogues considered, and is detailed below for each in turn (Section 3.2).

3.1.4 Step 4 – nuclear exclusion

By definition, ULXs are off-nuclear sources, and so we attempt to exclude sources that may be associated with the nuclei of their host galaxies. However, this is made challenging by the fact that low-luminosity active galactic nucleus (AGN) can exhibit similar luminosities to ULXs (Ghosh et al. 2008; Zhang et al. 2009). We therefore exclude potential AGN through their position relative to the centre of the galaxy instead, following the approach taken in Earnshaw et al. (2019b). In brief, for each X-ray source we compute the minimum separation from the central galaxy position, $R_{\rm min}$, based on its 3σ positional uncertainty (i.e. we define $R_{\rm min}$ = nuclear separation − 3σ position error). We then select sources with $L_{\rm X} > 10^{42}$ erg s^{-1}, as these sources are almost certainly AGN (only one ULX, ESO 243–49 HLX1, has exhibited such luminosities to date; Farrell et al. 2009), and calculate the cumulative distribution of their $R_{\rm min}$ values. Unsurprisingly, these typically exhibit very small minimum nuclear separations, and we determine the value of $R_{\rm min}$ that contains >99 per cent of these sources, which we take to be our exclusion criterion for nuclear sources, $R_{\rm min,excl}$ (see Section 3.2). All sources with $R_{\rm min} < R_{\rm min,excl}$ are subsequently excluded from our analysis. We repeat the assessment of $R_{\rm min}$ with both our input galaxy catalogue, where we have a requirement for a minimum amount of information regarding the extent of the galaxy (Section 2), and also with the full HyperLEDA/CNG/Cosmicflows galaxy catalogues (as for this stage, only the position of the galaxy is required), such that sources with $R_{\rm min} < R_{\rm min,excl}$ for *any* galaxy included in these data bases are excluded from our source lists. This empirical approach allows us to conservatively account for the uncertainty associated with the fact that for some galaxies it can be difficult to precisely identify its central/nuclear position (e.g. irregular or merging galaxies, and/or offset nuclei).

3.1.5 Step 5 – removal of other known contaminants

In addition to the nuclei of the apparent host galaxies for our sources, we also attempt to remove other known contaminants. At this stage, we particularly focus on background AGNs and foreground stars that coincidentally appear to be associated with a host galaxy in projection. We therefore positionally match our remaining source lists against lists of known stars and quasars. For the former, we use the Tycho2 catalogue (Høg et al. 2000) while for the latter we use the GAIAunWISE quasar catalogue (Shu et al. 2019) and the quasar catalogue of Véron-Cetty & Véron (2010). The search radii we use vary depending on the X-ray archive, as detailed in Section 3.2. Any source that matches with either a known star or a known quasar is excluded from our analysis.

3.2 Specific catalogue details

3.2.1 4XMM-DR10

The 4XMM catalogue (Webb et al. 2020) is formatted such that every row entry represents a unique detection of an X-ray source by the EPIC detectors (pn, MOS1, MOS2; Strüder et al. 2001; Turner et al. 2001), meaning that the observation-by-observation information needed to determine the peak flux for sources that have been observed on multiple occasions is already incorporated. For the initial position match (step 1), we specifically use the RA_SC and DEC_SC columns in the 4XMM catalogue for the X-ray position, which give the catalogue-averaged position for sources that have been detected on multiple occasions. 4XMM includes both point sources and extended sources, and we exclude observations in which the detection is marked as extended.[1] When computing detection luminosities (step 2), we use the full band flux provided in the catalogue (i.e. 4XMM band 8, spanning 0.2–12.0 keV); these fluxes are computed by summing the fluxes of the 4XMM sub bands, which are themselves computed assuming a standard spectral

[1]Note that we primarily use the observation-by-observation measures of source extent here, as opposed to the mission averaged measure (SC_EXTENT), as variable/transient point sources embedded in diffuse emission can still mistakenly be flagged as extended in the latter. As such, there are some sources included that have non-zero values for SC_EXTENT, but we stress that we have inspected the *XMM–Newton* images from the observations listed as being point-like for these sources that are included in our final sample, and visually confirmed the presence of a point-like source.

shape (an absorbed power-law continuum with $\Gamma = 1.7$ and $N_{\rm H} = 3 \times 10^{20}$ cm^{-2}).

For the quality flags (step 3), we largely follow the approach taken in Earnshaw et al. (2019b). In brief, detections with a summary flag $\geq$2 are excluded to reduce spurious detections in general, and sources with the out-of-time event flag (Flag 10) set and a total count rate < 0.05 ct s^{-1} are also excluded as these are likely to be artefacts of out-of-time events that are associated with a nearby bright source. However, in addition to these cuts, we also filter out entries where the MASKFRAC flag (Flag 1) is set to be true for each of the EPIC detectors that registered the detection. This helps to further limit spurious detections seen at chip edges, and also spurious 'new' detections at the edge of the field of view (FoV) that are really associated with known bright sources just outside the FoV. When filtering out sources consistent with being the nuclei of the host galaxies (step 4) and identifying likely matches with known foreground stars/background quasars, we again make sure to use the RA_SC and DEC_SC columns for the X-ray positions. For the former, we find $R_{\rm min,excl} = 9$ arcsec following the empirical approach described above. This is a pretty conservative cut, compared to previous works involving *XMM–Newton* data (Walton et al. 2011b; Earnshaw et al. 2019b). In the latter case, since we are simply matching point-source positions, we use a matching radius for the various star/quasar catalogues of 5 arcsec, roughly corresponding to the typical 3σ positional accuracy for point sources in 4XMM-DR10 (Webb et al. 2020).

3.2.2 2SXPS

By definition the 2SXPS catalogue (Evans et al. 2020b) only includes point sources detected by the XRT (Burrows et al. 2005), and the main table of the catalogue is formatted such that every row entry represents a unique X-ray source, with the observation-by-observation detection information contained in a separate table. However, the primary source table includes information on the peak flux seen by the XRT for each source included, and so we mainly use this table for our analysis. As such, for the initial position match (step 1), we are naturally using the best-fitting position determined from all of the available observations of a given source. When computing the relevant source luminosity (step 2), we primarily select sources based on the peak flux given for each source in the full XRT band (spanning 0.3–10.0 keV) assuming again an absorbed power-law continuum (fluxes for various potential spectral models are provided, but of these the absorbed power law is the most appropriate choice for ULXs below 10 keV). Here, the power-law parameters adopted when computing the catalogued fluxes are either fit directly, derived from the 2SXPS hardness ratios, or a photon index of $\Gamma = 1.7$ and the Galactic column in the direction of the source are assumed (see Evans et al. 2020b for details).

In contrast to both *XMM–Newton* and *Chandra*, typical *Swift* observations are very short exposures ($\sim$1–2 ks). Furthermore, these observations themselves are often split up into several shorter 'snapshots', and the peak flux included in the catalogue can in principle be drawn from the count rate seen during one of these snapshots instead of the full observation. As such, the peak flux often has large uncertainties, being based on only a handful of counts. For sources where the peak luminosity has a fractional error of >40 per cent (averaging the positive and negative errors quoted), corresponding to a detection with $\sim$10 counts based on the approximation for the Poisson distribution presented in Gehrels (1986), we therefore also require that the source meet at least one of three additional criterion for inclusion. Either: (1) the average luminosity is also consistent with the ULX regime, assuming that the average and peak luminosities are not identical, or (2) there are two or more independent detections of the source in the ULX regime, based on the observation-by-observation data, or (3) the source has also previously been detected in the ULX regime by some other facility (i.e. the detection is spatially consistent with an entry in one of the archival ULX catalogues we compare our new data set against; see Section 4.1 for further discussion). For the quality flag cut (step 3), we exclude sources with the summary flag set to $\geq$1 (i.e. the 'clean' criterion defined by the *Swift* team). When filtering out sources consistent with being the host galaxy nuclei (step 4), we also find $R_{\rm min,excl} = 9$ arcsec, similar to our analysis of 4XMM. Finally, when identifying likely matches with known foreground stars/background quasars (step 5), we use a matching radius of 10 arcsec for the *Swift* data, again corresponding to the typical 3σ positional accuracy for sources in 2SXPS (Evans et al. 2020b).

3.2.3 CSC2

Similar to 2SXPS, the main table of the CSC2 catalogue (Evans et al. 2020a) is formatted such that every row entry represents a unique X-ray source, with the observation-by-observation detection information presented in a separate table, and similar to 4XMM both point-like and extended sources are included. We therefore use the primary source table when performing the initial position match with our galaxy catalogue (step 1), such that we are again using the best-fit position determined from all of the available observations of a given source, but we then compile the observation-by-observation information for each matched source from the secondary table so that we can be sure to account for the peak flux seen by *Chandra* for each source in our analysis. Sources listed as being extended are discarded. When computing detection luminosities (step 2), we use the broad-band CSC2 fluxes, i.e. 'broad' fluxes for the ACIS detectors (Garmire et al. 2003), spanning 0.5–8.0 keV, or 'wide' fluxes for the HRC (Zombeck et al. 1995), spanning 0.2–10.0 keV. Where possible we again use fluxes derived assuming a power-law spectral form (as with 2SXPS, fluxes for a variety of spectral models are provided, see the CSC2 documentation for details). Here, the catalogued power-law fluxes we use are computed assuming $\Gamma = 2$ and the appropriate Galactic column. However, if this power-law flux is not available then we use the raw aperture flux instead. For the quality flag cut, we only consider sources which are flagged as 'true' detections in the primary source table (i.e. sources flagged as 'marginal' detections are excluded), and we also exclude source detections at the observation level for which the 'streak' flag is set.

In addition to the standard filtering steps outlined above, one further issue that is of relevance for the observation-by-observation *Chandra* data is the fact that the *Chandra* PSF degrades rapidly with off-axis angle (in a relative sense, much more severely than is the case for either *XMM–Newton* or *Swift*). As such, the typical extraction radii used in CSC2 also increase with increasing off-axis angle; for example, sources with off-axis angles of $\sim$8 arcmin often have extraction radii of $\sim$9–10 arcsec, significantly larger than the on-axis PSF. Unfortunately, for point sources that are either in crowded regions or are embedded in extended regions of diffuse emission, this can result in spurious fluxes for any significantly off-axis observations, as these off-axis detections can occasionally be blends of multiple point sources, and/or include significant diffuse flux not actually associated with the point source in question. This is particularly an issue for observations of nearby giant elliptical

galaxies; *Chandra* has undertaken significant programmes tiling a number of these galaxies (e.g. M87) resulting in a combination of on- and off-axis observations of the same crowded fields. As such, there are a number of sources in these galaxies that have very modest luminosities when viewed on-axis ($L_X < 10^{38}$ erg s^{-1}) but that all appear to share the same ULX-level off-axis detection. Although some ULXs can be highly variable, as noted above, in many of these cases the ULX-level detections are unfortunately spurious. We therefore manually inspect cases where the only ULX-level detection is taken significantly off-axis, and there is also an on-axis observation that shows the source to have a significantly lower luminosity. Where these are clearly cases relating to source confusion, we exclude these sources from our analysis. We also exclude cases in which the size of the aperture increases to the point where it covers the nominal position of the galaxy centre. In cases where the higher flux could plausibly be due to variability (i.e. the on-axis observations show no evidence for large numbers of sources or diffuse emission whose integrated flux could explain that seen in the off-axis observation), we retain these detections, but stress that they should be considered high-priority for further (triggered) follow-up to confirm their nature. We also retain cases in which the aperture marginally overlaps with the edge of the nuclear exclusion zone (but not the nominal nuclear position).

When filtering out sources consistent with being the host galaxy nuclei (step 4), we find $R_{\rm min,excl} = 6.1$ arcsec for CSC2, smaller than the equivalent value for both 4XMM and 2SXPS. Although in a qualitative sense this is not surprising, given the superior imaging capabilities, it is still worth noting that this value is still significantly larger than the *Chandra* point spread function. This likely reflects the fact that for more complex galaxy morphologies it can be difficult to accurately identify the position of the true galaxy centre. Finally, when identifying likely matches with known foreground stars/background quasars (step 5), we use a matching radius of 3 arcsec.

3.3 Merging and further filtering

Once all of the individual catalogues of ULX candidates from each of the 4XMM-DR10, CSC2, and 2SXPS archives have been produced, we merge them all into a final 'master' ULX catalogue. To do so, we sequentially match our individual *XMM–Newton*, *Swift*, and *Chandra* catalogues of ULX candidates by position. We begin by matching the *XMM–Newton* and *Swift* catalogues. As *Swift* is typically the limiting factor regarding position uncertainties, we match the two within a radius of 10 arcsec, corresponding to the typical 3σ 2SXPS position uncertainty. There are three main outcomes from this initial match: sources with only *XMM–Newton* data, sources with only *Swift* data, and matched sources with both. Each of these lists are then matched with the *Chandra* catalogue. For the sources with only *Swift* data, we again use a matching radius of 10 arcsec here, and for the sources with only *XMM–Newton* data we use a matching radius of 5 arcsec (again, the typical 3σ 4XMM-DR10 position error, as *XMM–Newton* is the limiting factor regarding position uncertainties here). For sources with both *XMM–Newton* and *Swift* data, we assume the *XMM–Newton* position to be more accurate, and so use this to match to the *Chandra* catalogue, again using a matching radius of 5 arcsec.

At each of these matching stages, there is the possibility that there are multiple matches for the same source. This is particularly the case when matching either the *XMM–Newton* or the *Swift* data with *Chandra*, given the potential for source confusion and the superior imaging capabilities of the latter; a famous example is the case of NGC 2276, in which a source perceived to be an extremely luminous ULX by *XMM–Newton* is actually resolved into three distinct point sources by *Chandra* (Sutton et al. 2012). In that case, all of the resolved sources are themselves ULXs, but it is also possible that a source that appears as a ULX to *XMM–Newton* or *Swift* will actually be resolved into multiple sub-ULX sources (this is conceptually similar to the issue regarding the degradation of the off-axis *Chandra* PSF discussed in Section 3.2.3). In addition to matching them against our *Chandra* catalogue of ULX candidates, we therefore also match our *XMM–Newton* and *Swift* ULX candidates against the set of *Chandra* sources that did not make our luminosity cut, and again manually inspect all cases of multiple matches in order to identify sources that only appear to be ULXs because of a detection that is actually likely the blend of several point sources, artificially inflating its apparent flux. As before, these sources are removed from our analysis. We note, however, that we still retain cases where e.g. *Chandra* resolves an *XMM–Newton* detection into two discrete sources, but that the *XMM–Newton* data imply that at least one of these must have varied into the ULX regime (for example, a scenario in which *Chandra* sees two sources at $L_X \sim 10^{38}$ erg s^{-1}, but the *XMM–Newton*/*Swift* detection that is consistent with both of these sources implies $L_X \sim 2 \times 10^{39}$ erg s^{-1}, meaning that at least one of these sources must have been in the ULX regime during the *XMM–Newton*/*Swift* observation). In these cases, we add a flag to the final version of the master catalogue noting that this issue exists (a separate flag is added for each of the matched catalogue pairs, see Table 1 for the definitions of the different values these flags can take).

On occasion, where there are multiple matches it is possible to determine with reasonable confidence which of the resolved sources the unresolved detection is actually associated with (for example, cases where *Chandra* sees two sources, one with $L_X \sim 10^{38}$ erg s^{-1} and one with $L_X \sim 10^{40}$ erg s^{-1} and *XMM–Newton*/*Swift* sees one source that also has $L_X \sim 10^{40}$ erg s^{-1}, or alternatively cases in which the position of the first *Chandra* source is in outstanding agreement with the position of the *XMM–Newton*/*Swift* detection, while the second *Chandra* source is right at the edge of the 3σ uncertainty range). In these cases, we make a judgement call ourselves and assign the unresolved detection to the resolved source we feel is most appropriate. Where we feel unable to make a judgement, but there are multiple ULX candidates among the resolved sources (similar to the case of NGC 2276 highlighted above), we retain all of the potential resolved matches within the master catalogue. Both of these scenarios are also indicated by the matching flags highlighted above (again, see Table 1).

Table 1. Definitions for the flags detailing the decision taken for any complex matches between the individual ULX catalogues.

Value	Description
NULL	No match between the catalogues
0	Unique match between ULX candidates
1	Formally more than one potential match between ULX candidates, but one is clearly preferred and assumed to be the correct match; only this match is reported
2	Formally more than one potential match between ULX candidates, and it is unclear which is the correct association; all potential matches are given
3	ULX detection consistent with several lower luminosity sources seen by the other mission in question, but their combined flux is not sufficient to explain that seen of the ULX detection, so the source is still retained

Having merged the *XMM–Newton*, *Swift*, and *Chandra* data as best we can, we now address the presence of one more class of known contaminants, X-ray transients associated with one-off explosive events (i.e. supernovae). Although certainly not all do, these events can reach ULX luminosities, and would then be selected by our process (given our interest in genuinely transient ULXs) even though they are clearly not accretion-powered X-ray binaries. This is particularly relevant here given our use of *Swift* data, since one of *Swift*'s main focuses is rapid follow-up of transient events. We therefore correlate our master catalogue with the positions of known supernovae recorded in the Open Supernova Catalogue (Guillochon et al. 2017; note that this includes both supernovae that have occurred since *XMM–Newton*, *Chandra*, and *Swift* have been observing and more historic supernovae). To do so, we prioritize X-ray source positions from *Chandra*, *XMM–Newton*, and *Swift* in that order (i.e. in cases where a source is detected by all three observatories, we use the *Chandra* position for this match), and perform the match using search radii of 3, 5, and 10 arcsec for *Chandra*, *XMM–Newton*, and *Swift* positions, respectively. However, in order to determine whether the X-ray source is really associated with the transient in question we also examine the relative timing of the event and the first detection of the X-ray source (hence our decision to only apply this filter to the merged data set, where we can most robustly determine when the source was first detected). X-ray sources that are positionally coincident with supernovae, but which were detected as ULXs significantly before the event occurred are deemed to be unrelated to the supernova and retained in our sample. However, sources positionally coincident with known transients that have only been detected after the event occurred are assumed to be associated with the supernova, and so are excluded from our final sample.

We also match our remaining sample against both the NED and SIMBAD data bases in order to identify and remove any further non-ULX contaminants that have been identified in the literature (uncatalogued AGNs, stars, and supernovae). We adopt the same spatial matching procedure as for the Open Supernova Catalogue, prioritizing *Chandra*, *XMM–Newton*, and *Swift* positions in that order and using matching radii of 3, 5, and 10 arcsec. For any further supernovae identified, we also again consider the date of the first X-ray detection when deciding whether the X-ray source should be removed. We then remove any remaining sources obviously associated with the host-galaxy AGNs that have been missed by our nuclear cut (e.g. sources with $L_X \geq 10^{42}$ erg s^{-1} that lie just outside our nuclear exclusion radii or, in the case of Centaurus A, are located in the X-ray emission from the AGN jet; Hardcastle et al. 2007) as well as a number of sources for which we are aware of follow-up studies that have previously found the ULX candidate to be an uncatalogued background quasar/foreground star (Dadina et al. 2013; Heida et al. 2013; Sutton et al. 2015; Guo et al. 2016).

Finally, after all of the above steps, we find that the remaining sample contains a number of highly clustered sources which only appear in 2SXPS and actually seem to be associated with the bright diffuse emission known to be present in the M82 galaxy (e.g. Griffiths et al. 2000; Lopez et al. 2020), even though 2SXPS is intended to be a dedicated point source catalogue. This is likely related to the typical snapshot nature of *Swift* XRT observations; with such short exposures random Poisson fluctuations from the diffuse emission may more easily be mistaken as point sources. 2SXPS notes all of the potential aliases for each entry, and many of these M82 sources are listed as potentially being aliased with each other. We therefore also manually inspect X-ray images – both the images integrated over the duration of the *Swift* mission and specifically taken from the observation corresponding to the reported best detection for the XRT, and, where available, any CSC2 *Chandra* images as well – for all of the 2SXPS sources which have not also been identified as a ULX candidate in either of our 4XMM-DR10 or CSC2 subsamples and are listed as having other potential 2SXPS aliases. Any sources which we judge to be likely associated with diffuse emission (similar to the M82 case) are removed from the final sample. During this process, if a source is aliased with another genuine point source (as opposed to being part of a cluster of sources associated with extended emission), we also make a judgement over whether these are likely the same source, and retain only one entry in these cases.

4 THE FINAL SAMPLE

Our final sample of ULX candidates consists of 1843 individual sources residing in 951 host galaxies. The catalogue will be made available to the public, and will be comprised of four tables. The first is a 'master' list formatted to have one row entry per source, summarising some key information and detailing which combination of *XMM–Newton*, *Swift*, and *Chandra* have reported the source as a ULX. We stress that we are focused only on the detections of these sources that meet the ULX luminosity threshold here (i.e. $L_X \geq 10^{39}$ erg s^{-1}); if an *XMM–Newton* ULX candidate does not have a *Chandra* counterpart reported, for example, this does not necessarily mean that *Chandra* has not detected that source, only that *Chandra* has not seen it at a flux that would correspond to the ULX regime. The other three tables provide the full details of the 4XMM-DR10, 2SXPS, and CSC2 entries for the ULX-level detections of these sources. These follow the formats of the data used to compile these subsamples of ULX candidates in the first place (i.e. the *XMM–Newton* and *Chandra* tables have one row entry per observation of a ULX candidate, while the *Swift* table just has one row entry per ULX candidate).

Some statistics for the full sample and the individual 4XMM-DR10, 2SXPS, and CSC2 sub-samples are given in Table 2, and we show examples of our source selection in Fig. 2 for each of the *XMM–Newton*, *Swift*, and *Chandra* observatories. By number, the CSC2 component contributes the most sources to our final sample, followed by 4XMM-DR10 and then 2SXPS. The latter still makes a very significant contribution though. There is obviously notable overlap between the individual subsamples (i.e. some sources are detected as ULXs by multiple missions), as also detailed in Table 2 and in the master table provided. Of our 1843 individual sources, 50 are detected at ULX luminosities in all three of our contributing source catalogues.

As expected, given the known connection between ULXs and recent star formation (Swartz, Tennant & Soria 2009; Mineo, Gilfanov & Sunyaev 2012; Lehmer et al. 2019), the majority of our ULX host galaxies with morphology information available are spiral galaxies (∼60 per cent, using the T-type ranges defined above). We also plot the distribution of host galaxy distances in Fig. 3 for the full sample and each of the individual catalogue subsamples. There is significant overlap in the individual distributions, but typical host galaxy distances are lowest for the 2SXPS subsample, and largest for the CSC2 subsample, as the latter has the best sensitivity to faint point sources among the X-ray catalogues considered owing to both the low background and superior imaging capabilities of *Chandra*. This allows *Chandra* to more easily detect ULX candidates out to larger distances than either *XMM–Newton* or *Swift*, and thus the CSC2 subsample ends up making the largest contribution to our final sample.

Of our 951 host galaxies, 333 are found to host multiple ULX candidates. As our primary interest is focused on individual sources,

Table 2. The final sample of ULX candidates compiled from the 4XMM-DR10, 2SXPS, and CSC2 catalogues.

	4XMM-DR10	2SXPS	CSC2	Combined sample
Number of ULX candidates	641	501	1031	1843
(with multiple ULX detections in the parent catalogue)	177	291	246	702
(seen as a ULX by multiple observatories)	241	173	209	293
(HLX candidates)	22	36	17	72
Host galaxies	403	269	548	951
(average distance, Mpc)	62.3 ± 3.5	34.8 ± 2.7	83.8 ± 3.8	74.7 ± 2.7
(containing multiple ULX candidates)	130	89	190	333

and our sample selection is highly non-uniform, we do not make any attempt to correct for (in)completeness in any galaxies observed with insufficient depth to reach luminosities of 10^{39} erg s^{-1}, so this should likely be considered a lower limit for ULX multiplicity in these hosts. The most extreme example is NGC 2207 – one-half of an interacting galaxy pair (the other being IC 2163; Eskridge et al. 2002) – which appears to host an astonishing 34 ULX candidates, the majority of which (31) are contributed by the CSC2 catalogue. This is notably larger than the 21 ULXs reported to reside in NGC 2207/IC 2163 by Mineo et al. (2013), likely due to additional *Chandra* observations being included in CSC2 and our explicit consideration of long-term variability in selecting our ULX sample. Owing to the interacting nature of these galaxies, it is not surprising that there should be a large number of ULXs. It is nevertheless worth noting that there seems to be some disagreement over the distance to NGC 2207 in the literature. The distance we have adopted here is $D = 36.4$ Mpc, which is based on the recession velocity reported in HyperLEDA. This distance is very similar to that reported based on the supernova SN1975A which occurred in NGC 2207 ($D = 39.6$ Mpc; Arnett 1982), which is adopted by Mineo et al. (2013). However, the more recent estimates from the Tully–Fisher method typically seem to imply a distance of $D \sim 17$ Mpc (Russell 2002; Theureau et al. 2007). Should this be correct, only 7 of our sources in NGC 2207 would still be considered ULXs. However, our assumption is that the supernova-based distance is the most reliable here, and so our luminosity estimates should be reasonable.

We also note that among the 1843 ULX candidates, our catalogue contains 72 'hyperluminous' X-ray source (HLX) candidates.[2] These are the most extreme members of the ULX population, exhibiting luminosities of $L_X \geq 10^{41}$ erg s^{-1}. Owing to their astonishing luminosities, such sources are often considered the best candidates for IMBH accretors. Indeed, two of the sources discussed as the leading IMBH candidates in the literature, M82 X-1 and ESO 243–49 ULX1, are found among this population. However, it is also worth noting that one of the known ULX pulsars, NGC 5907 ULX1, also reaches luminosities of $L_X \sim 10^{41}$ erg s^{-1} (Fürst et al. 2017; Israel et al. 2017a), despite being powered by a neutron star. Nevertheless, these sources are still of particular interest, and our new HLX candidates will be discussed in more detail in future work (A. D. A. Mackenzie, et al., in preparation).

[2]Note that in order for sources detected in 2SXPS to be considered good HLX candidates we apply a similar criterion to our initial source selection procedure, such that if the peak luminosity is not well constrained (average fractional uncertainty of >40 per cent) then the source has to have either a better-constrained average luminosity that is also in the HLX regime, or at least two separate XRT observations that place it in the HLX regime.

4.1 Comparison with other ULX catalogues

The first major effort to search for ULXs among any of the X-ray source catalogues considered here was presented by Kovlakas et al. (2020), who also searched CSC2 for ULX candidates. Although both the approach taken and the input galaxy sample used are quite similar in both cases, there are also a couple of notable differences. First and foremost, we have considered the *Chandra* data down to the observation-by-observation level, in order to select sources based on their peak flux and specifically include transient ULXs in our sample, while Kovlakas et al. (2020) base their luminosity selection on the flux recorded in the longest uninterrupted segment of *Chandra* data (which is not necessarily the peak flux exhibited by the source). Secondly, we have taken a much more conservative approach to excluding potential nuclear sources associated with our host galaxies. Kovlakas et al. (2020) flag a source as 'nuclear' if it is within 3 arcsec of the nominal galaxy centre, while we both consider the position error on the X-ray detection and utilize a much larger minimum exclusion radius (6.1 arcsec). This is based on our empirical assessment of the separation between the nominal centre of the host galaxies and sources that we consider likely to be their AGN (those that appear to have $L_X \geq 10^{42}$ erg s^{-1}). Our more conservative approach does mean that our catalogue is likely cleaner with regards to any remaining contamination from AGN in our host galaxies, but this will come at the cost of excluding a larger number of *bona fide* ULXs from our sample, particularly given that the spatial density of ULXs is seen to increase towards the galaxy centres (Swartz et al. 2011; Wang et al. 2016; Kovlakas et al. 2020). Nevertheless, this is a more appropriate approach given that our primary motivation is to find individual sources that are of interest for follow-up studies; detailed follow-up of ULXs within a few arcseconds of the nuclear position will not realistically be feasible for the majority of our current and planned X-ray facilities if the nuclear black hole is even reasonably active. Despite these differences, though, there is naturally a fairly significant degree of overlap (754 sources) between our sample and sources that would qualify as ULXs in Kovlakas et al. (2020).

More recently, Inoue, Yabe & Ueda (2021) have also searched for CSC2 for ULX candidates. However, a major difference between these works is that Inoue et al. (2021) have used a much smaller catalogue of input galaxies than that used here, derived by combining IRAS galaxies with the CNG catalogue. Furthermore, while they do consider the observation-by-observation data provided in CSC2, they use the flux from the longest individual observation when computing luminosities, which again is not necessarily the peak flux exhibited by the sources in question (which is what we are interested in here), and we have again been more conservative in our treatment of nuclear sources. Although their work primarily focuses on CSC2, the final catalogue does also include sources selected from 4XMM-DR9 and 2SXPS, and so is therefore conceptually similar to our multimission

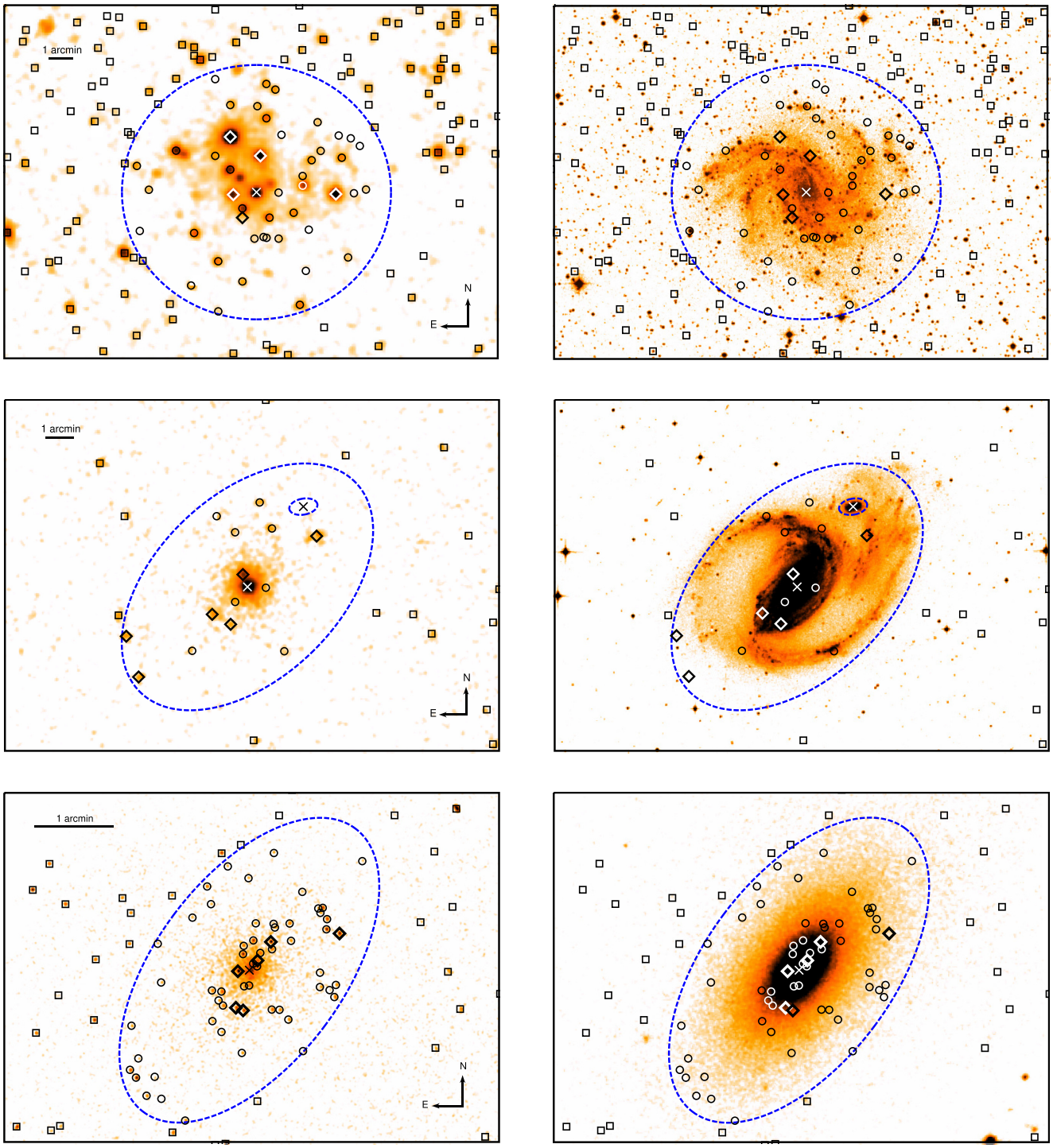

Figure 2. X-ray (*left*) and accompanying optical (*right*) images for three example galaxies that demonstrate some of the main stages of our source selection. For the X-ray images, from top to bottom, we show an *XMM–Newton* EPIC image of NGC 6946 (OBSID 0691570101), the integrated *Swift* XRT image of NGC 1097 (generated with the standard online XRT pipeline; Evans et al. 2009) and a *Chandra* ACIS image of NGC 720 (stack ID acisfJ0153056m134345). All are smoothed with a Gaussian of width 3 pixels. The optical images are from the Digitized Sky Survey. In all panels, the D25 extent of the galaxy in question is indicated with the blue dashed ellipse, and the nuclear position with a cross (note that in the case of NGC 1097, the small companion galaxy NGC 1097A is also shown). 'Field' sources (i.e. outside of the D25 extent) are shown with squares, point sources within the D25 extent that do not qualify as ULX candidates with circles, and finally sources selected as ULX candidates are shown with diamonds, respectively; all markers are shown in either black or white simply so that they can most easily be seen against the background images, there is no further significance to the choice of colour. The *XMM–Newton* and *Chandra* images represent the deepest observation/stack of NGC 6946 and NGC 720 that are included in 4XMM-DR10 and CSC2, respectively. However, owing to the variable nature of the ULX population (see e.g. Earnshaw et al. 2019a for NGC 6946 in particular), not all sources identified as ULX candidates are necessarily visible in these X-ray images.

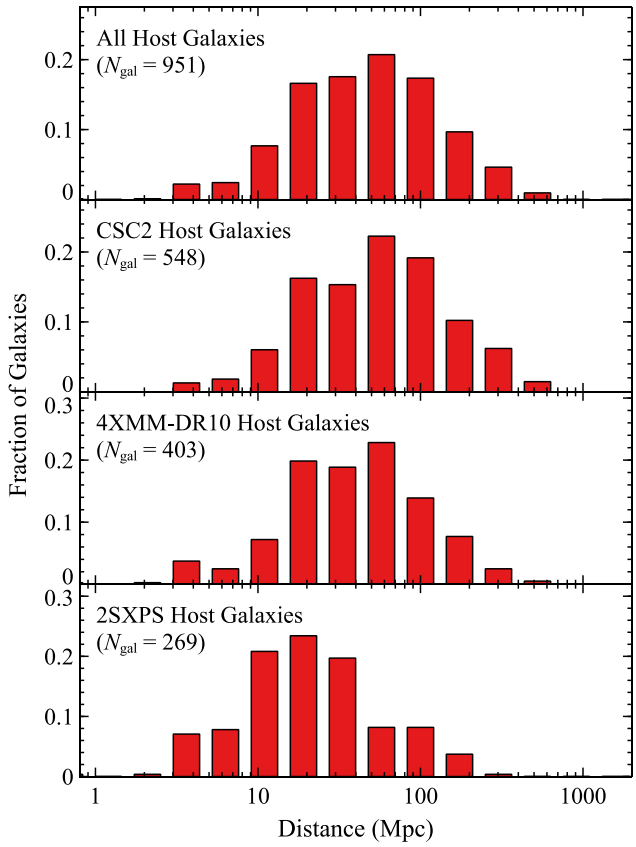

Figure 3. Distance distributions for ULX host galaxies, showing the full multimission sample (top), and the CSC2, 4XMM-DR10, and 2SXPS subsets, respectively (lower panels).

approach. There is not a lot of specific detail provided for these latter analyses, unfortunately, but the approach is stated to be broadly similar to that used for CSC2, and so similar differences between the two works are presumably present here too. In addition, another key difference with regard to the 2SXPS analysis is that they appear to have only made use of the average fluxes from *Swift*, while we have considered the peak flux (where this is considered reliable). Furthermore, we have used an even more recent release of the 4XMM survey here. Nevertheless, despite these differences, there is again some notable overlap of 357 sources in total (251, 107, and 149 from *Chandra*, *XMM–Newton*, and *Swift*, respectively).

Finally, Barrows, Mezcua & Comerford (2019) also utilize CSC2, but only search specifically for HLXs within the SDSS-DR7 galaxy sample. However, the spatial offsets relative to the central galaxy positions would result in the majority of their HLX candidates being considered as nuclear sources with our more empirical approach to this stage of the catalogue production. Only one of our sources is also present in the Barrows et al. (2019) catalogue, 2CXO J155910.3+204619, and we have assigned this to a different (and closer) host galaxy, giving it a much more modest luminosity of $L_X \sim 2.5 \times 10^{39}$ erg s^{-1}. As such, our sample of HLX candidates differs entirely to that presented by Barrows et al. (2019).

In addition to these more recent works, we also match our new catalogue against a series of other archival ULX catalogues, which have been derived using previous generations of X-ray surveys. In these cases we match by position, as they are not drawn from any of the exact X-ray catalogues used here (and thus do not have identical naming conventions). Similar to our final matching against the NED and SIMBAD for remaining contaminants, we split our ULX catalogue into sources where the best position comes from *Chandra*, from *XMM–Newton* and from *Swift*, and then individually match these sub-sections against each of the archival ULX catalogues in turn. The matching radius used for each comparison depends on the origins of the data being compared, and always corresponds to the larger of the typical positional uncertainties associated with the two input tables. As before, positions from *Chandra*, *XMM–Newton*, *Swift*, and *ROSAT* are considered to have typical uncertainties of 3, 5, and 10 arcsec, respectively, and *ROSAT* positions are considered to have a typical uncertainty of 20 arcsec. For example, when comparing the subset of our catalogue with *Chandra* positions against another catalogue derived from *Chandra* data, we would use a matching radius of 3 arcsec, but comparing the same subset against a catalogue derived from *ROSAT* observations, we would use a matching radius of 20 arcsec instead. For this analysis, we simply note all potential matches. The catalogues we match against are listed in Table 3.

Based on all of these matches, we find that 689 of the ULX candidates presented here are completely new, i.e. do not seem to appear in any of the other ULX catalogues considered, and 1318 have only recently been catalogued as a ULX, i.e. they only appear in catalogues based on the latest generation of X-ray source catalogues (Barrows et al. 2019; Kovlakas et al. 2020; Inoue et al. 2021; this work). Of these 'new' and 'recent' ULX candidates, 48 and 59, respectively, are HLX candidates. We stress that even if a source is considered 'new' in this respect, this does not necessarily mean the sources are completely unknown, only that it has not been formally catalogued as a ULX previously. For example, NGC 300 ULX1 is considered 'new' here, even though this source is one of the few known ULX pulsars (Carpano et al. 2018), and as such has received significant individual attention (Vasilopoulos et al. 2018, 2019; Kosec et al. 2018b; Walton et al. 2018a; Heida et al. 2019).

4.2 Estimation of unknown contaminants

Although we have taken significant measures to try and remove known contaminants, these processes can never be perfect, and so we stress that there will still be a significant contribution of sources that are not actually ULXs in our final sample of ULX candidates. By far the majority of these will be foreground/background sources that coincidentally appear to be associated with the host galaxies in question in projection, but have just not been formally identified/catalogued as such in the databases we have utilized (and thus have not been removed by our effort to identify and exclude these sources). Although we cannot remove these sources, it is still important to quantify their likely contribution.

In order to do so, we broadly follow the approach taken in Walton et al. (2011b), and subsequently Sutton et al. (2012) and Earnshaw et al. (2019b). This involves a calculation of the total expected number of sources that would be resolved from the cosmic X-ray background (CXB) given our selection criterion, the sensitivity of the observations from which the 4XMM, 2SXPS, and CSC2 X-ray catalogues have been generated, and the full set of galaxies in our catalogue that have been covered by the observations that contribute to these X-ray catalogues (not just those galaxies that have ULX detections). These estimates are then compared to the number of sources remaining in our catalogue, after accounting for the number of identified foreground/background sources that have already been filtered out, in order to estimate the remaining fractional contribution from these contaminants.

In order to estimate the total expected number of contaminants, we make use of empirically determined forms of the $N(>S)$ curves which

Table 3. Details of the archival ULX catalogues against which our new archive is compared.

Catalogue	Primary source and notes
Colbert & Ptak (2002)	*ROSAT*
Swartz et al. (2004)	*Chandra*
Liu & Bregman (2005)	*ROSAT*
Liu & Mirabel (2005)	Literature (incl. *ROSAT*, so positions treated as having *ROSAT* accuracy)
Liu (2011)	*Chandra*
Swartz et al. (2011)	*Chandra*
Walton et al. (2011b)	*XMM–Newton* (specifically 2XMM)
Gong et al. (2016)	*Chandra* (only $L_X \geq 3 \times 10^{40}$ erg s^{-1})
Earnshaw et al. (2019b)	*XMM–Newton* (specifically 3XMM-DR4)
Barrows et al. (2019)	*Chandra* (specifically CSC2 HLXs)
Kovlakas et al. (2020)	*Chandra* (specifically CSC2)
Inoue et al. (2021)	Mainly *Chandra* (specifically CSC2), but also includes *XMM–Newton* and *Swift* (specifically 4XMM-DR9 and 2SXPS)

quantify the number of sources per square degree (N) resolved from the CXB as a function of flux sensitivity (S). These are combined with observational sensitivity maps in order to estimate the number of background sources each galaxy in our input sample that has been observed should contribute. Sensitivity maps for the observations from which the 4XMM and CSC2 catalogues are compiled are provided as part of these data releases, but are not available for the 2SXPS catalogue at the time of writing. We therefore focus our calculations on the 4XMM and CSC2 data, performing this calculation for each data set separately; as will be clear below, the expected level of contamination for these data sets are very similar, and so we still expect these results to hold overall.

For CSC2, since the initial source detection is performed using 'stacks' of observations (a stack is defined as a group of observations for which the aimpoints are all within 1 arcmin; see the CSC2 documentation), we use the sensitivity maps generated for these stacks in our analysis. These are provided for all of the energy bands considered in the CSC2 catalogue. However, as noted by Walton et al. (2011b), owing to absorption in the apparent host galaxies (which lie between us and any background AGN) these calculations are most robust at higher energies, and so we limit ourselves to the hard band (2–7 keV) ACIS maps that correspond to the 'true' detection threshold to match our data selection (the HRC makes a negligible overall contribution here). We also make use of the $N\,(>S)$ curves recently published by Masini et al. (2020), who present an expression for the same 2–7 keV band.

There are two limiting fluxes to consider here. The first is set by our selection of sources that appear to have $L_X \geq 10^{39}$ erg s^{-1}. For each galaxy we work out the hard band flux that would correspond to a broad-band luminosity of 10^{39} erg s^{-1}, S_{ulx}, based on the distance to the galaxy and the fraction of the broad-band flux that would appear in the hard band. We use a coarse representation of the average spectral shape for ULXs below 10 keV (e.g. Stobbart et al. 2006; Gladstone et al. 2009; Pintore et al. 2017): an absorbed power-law spectrum with $\langle N_H \rangle = 3 \times 10^{21}$ cm^{-2} and $\langle \Gamma \rangle = 2.1$. The second flux is the limiting sensitivity of the stack in question, S_{obs}, provided by the sensitivity maps. The relevant limiting sensitivity for use with the $N\,(>S)$ curve is then the larger of these two values, such that if an observation is sensitive enough to detect sources at lower luminosities, these are not included in our estimated number of contaminants. For each of the galaxies covered by CSC2 we use the $N(>S)$ curve and the appropriate limiting sensitivity to compute maps of the number of expected background sources per pixel, and integrate these over the area of the galaxy covered by each relevant *Chandra* stack (excluding the typical area excised around the central galaxy location by our nuclear cut). For each of the galaxies covered by CSC2 data (again, not just those with ULX detections), we perform this calculation for every available stack. We then select the stack that would give the largest number of contaminants, and sum these values over all of the galaxies covered by CSC2 stacks to compute the total number of expected contaminants prior to the removal of any known foreground/background sources. From this, we compute the remaining fractional contamination among the CSC2 ULX candidates by comparing the expected number of remaining contaminants to the number of ULX candidates detected in the hard band for self-consistency (i.e. excluding sources that only have upper limits).

For 4XMM, the sensitivity maps are only provided for the full band (0.2–12.0 keV) and are based on the combined sensitivity for all of the EPIC detectors (see section 9 in Webb et al. 2020). However, as stated above, it is preferable to work in the hard band here. Furthermore, suitable $N\,(>S)$ curves are not currently available for the full *XMM–Newton* bandpass; aside from work focusing specifically on *Chandra*, $N\,(>S)$ curves are determined almost exclusively for the 0.5–2.0 and 2–10 keV bands. It is therefore necessary to correct the results from the available broad-band maps to one of these bands, and we again choose the harder band, but this is not a trivial process. To do so, we also make use of the hard band (2–12 keV) sensitivity maps computed as part of the Earnshaw et al. (2019b) ULX catalogue for the majority of observations that make up 4XMM-DR10 (specifically those that make up 3XMM-DR4). However, these are computed using a different approach (see Carrera et al. 2007 and Mateos et al. 2008), consider each of the EPIC detectors separately, and adopt a different detection threshold (the hard band maps are computed for a $\sim 4\sigma$ detection in a single detector, while the broad-band maps are computed for a $\sim 3\sigma$ detection combining all the EPIC detectors), further complicating the situation.

For each galaxy covered by these earlier observations, we therefore process the available hard band sensitivity maps for each of the detectors in a similar manner as above, using the appropriate $N(>S)$ curve published by Cappelluti et al. (2009) but only considering for the limiting observational sensitivity (S_{obs}) for the time being, and note the results for the detector that predicts the largest number of contaminants. We also process the broad-band maps for the same observations by computing the fraction of the broad-band flux in both the softer (0.5-2.0 keV) and harder (2–10 keV) bands using the spectral form assumed in their generation (an absorbed power law with $N_H = 1.7 \times 10^{20}$ cm^{-2} and $\Gamma = 1.42$, typical for CXB sources), processing these updated maps in turn using the relevant $N(>S)$ curves, again only considering S_{obs}, and averaging the final results

to obtain an estimate for the number of contaminating sources the broad-band maps would imply. For each galaxy covered by these earlier observations, we then compare the results from the broad band and the hard band maps to compute an empirical correction for the former; we find this correction to be a factor of 9. We then process the full set of 4XMM-DR10 broad-band sensitivity maps using this correction to produce maps of the expected number of hard band CXB sources. At this point, we also consider the number of contaminants implied by the second limiting sensitivity, $S_{\rm ulx}$, and update the maps accordingly. Similar to before, we then integrate these maps over the galaxy area covered by every observation of that galaxy (again excluding the typical area around the central position excised by our nuclear cut, and again considering all galaxies covered by 4XMM-DR10) and pick the observation that gives the largest number of hard-band contaminants for each galaxy. We then sum these values to compute the total number of expected contaminants prior to the removal of any known foreground/background sources, and finally compute the remaining fractional contamination among the 4XMM ULX candidates (comparing the expected number of remaining contaminants against the number of ULX candidates that are detected at the 4σ level in any of the EPIC detectors for self-consistency).

Based on these approaches, and the numbers of known foreground/background contaminants already removed, we estimate fractional contaminations of (23 ± 2) per cent, and (18 ± 3) per cent for our CSC2 and 4XMM-DR10 ULX candidates, respectively (quoted uncertainties are due to counting statistics, and are 1σ). These values are sufficiently similar that, even though the relevant sensitivity maps are not yet available for 2SXPS, we still expect that an overall fractional contamination of $\sim$20 per cent is relevant for the whole catalogue.

5 NGC 3044 ULX1 – A NEW EXTREME ULX

The non-uniform selection means the full ULX sample presented here is not necessarily well suited for detailed statistical studies of the ULX population similar to those presented by Kovlakas et al. (2020) and Inoue et al. (2021). Indeed, our intention in compiling this sample is to facilitate follow-up studies of interesting individual sources. As such, in order to highlight the potential of our catalogue, we instead present a case study of a new extreme ULX candidate with $L_{\rm X,peak} \sim 10^{40}$ erg s^{-1} in the edge-on spiral galaxy NGC 3044 by both *Swift* and *XMM–Newton* (see Fig. 4). Although we have found several new HLX candidates in our analysis, we highlight this new source in particular both because of its luminosity is still very extreme, but also because it already has high signal-to-noise (S/N) *XMM–Newton* data (several thousand counts) available in the archive; as noted above, our new HLX candidates will instead be studied in future work (Mackenzie, in preparation). Hereafter, we refer to this source as NGC 3044 ULX1 for simplicity, as it is the brightest ULX candidate in NGC 3044, but its catalogued 4XMM-DR10 and 2SXPS IAU names are 4XMM J095343.8+013416 and 2SXPS J095343.7+013417, respectively. Throughout this analysis, we assume a distance of $D = 20.6$ Mpc to NGC 3044 (Tully et al. 2016).

5.1 Observations and data reduction

NGC 3044 has been observed on four occasions by *XMM–Newton*, and on five occasions by *Swift*. A log of these observations is given in Table 4. We primarily focus on the *XMM–Newton* observations here, but also process the *Swift* observations to provide further information on the long-term variability.

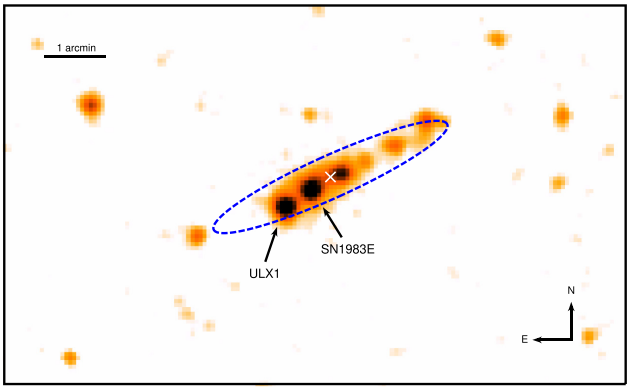

Figure 4. *XMM–Newton* image of NGC 3044 from OBSID 0782650101. As with Fig. 2, the D25 extent of NGC 3044 is shown with the blue dashed ellipse, and the nuclear position with a white cross. The positions of the brightest ULX candidate in NGC 3044, which we refer to as ULX1, and the nearby supernova 1983E are indicated.

Table 4. Details of the X-ray observations of NGC 3044 ULX1 considered in this work.

Mission	OBSID	Start date	Good exposure (ks)[a]
XMM–Newton	0070940101	2001-11-24	6/8
XMM–Newton	0070940401	2002-05-10	9/21
XMM–Newton	0720252401	2013-05-06	9/11[b]
Swift	00092188001	2015-04-17	1
Swift	00092188002	2015-04-19	1
Swift	00092188003	2015-06-23	2
Swift	00092188004	2015-06-24	2
Swift	00092188005	2015-06-25	2
XMM–Newton	0782650101	2016-12-07	80/93

[a] *XMM–Newton* exposures are listed for the EPIC-pn/MOS detectors, after filtering for background flaring (see Section 5.1).
[b] ULX1 falls on a dead chip for the MOS1 detector in this observation.

The *XMM–Newton* data for each observation are reduced following standard procedures using the *XMM–Newton* Science Analysis System (SAS v19.1.0). All of the *XMM–Newton* observations were taken in full-frame mode. Raw observation files for the EPIC-pn and EPIC-MOS detectors are cleaned using EPCHAIN and EMCHAIN, respectively. In order to facilitate pulsation searches, the cleaned EPIC-pn event files are corrected to the solar barycentre using the DE200 solar ephemeris, as this has the best time resolution of the *XMM–Newton* detectors (73.4 ms in full-frame mode). Source products are extracted from the cleaned event files with XMMSELECT. Given the relative proximity of supernova SN1983E (separated by $\sim$35 arcsec; see Fig. 4), we use circular source regions of radius 15–20 arcsec, with the larger region size used for the higher flux observations (see below). Background is estimated from a larger region of blank sky on the same detector as ULX1. All of the observations suffer from periods of enhanced background to some degree, and for each observation we determine the background threshold that maximizes the source S/N over the full *XMM–Newton* band considered in our more detailed analysis (0.3–10.0 keV) following the method outlined in Piconcelli et al. (2004). Only single and double patterned events are considered for EPIC-pn (PATTERN ≤ 4) and single to quadruple patterned events for EPIC-MOS (PATTERN ≤ 12), as

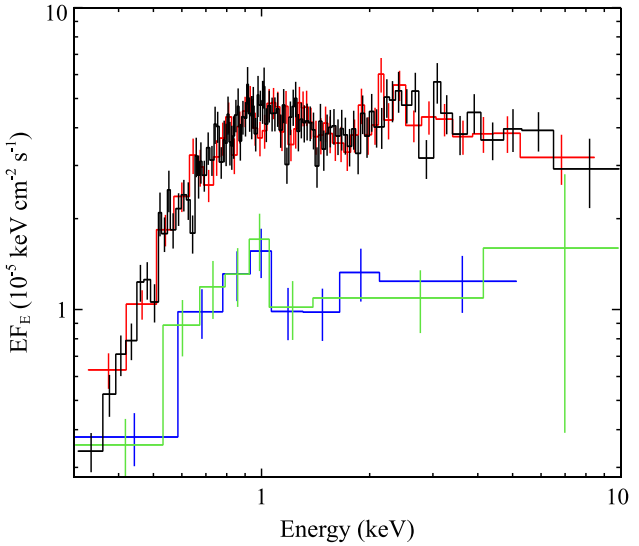

Figure 5. The *XMM–Newton* spectra of NGC 3044 ULX1 from the high- and low-flux states seen in the available data, unfolded through a model that is constant with energy. The EPIC-pn data are shown in black and green, and the EPIC-MOS data are shown in red and blue. The data have been rebinned for visual clarity.

recommended, and all of the necessary instrumental response files were generated using ARFGEN and RMFGEN. After performing the reduction separately for the two EPIC-MOS units, we combine their individual spectra using ADDASCASPEC.

5.2 Spectral analysis

Based on the 4XMM-DR10 data, the first two *XMM–Newton* observations (2001 and 2002) both caught NGC 3044 ULX1 in a lower flux state, while the latter two (2013 and 2016) caught the source in a higher flux state. We therefore combine the *XMM–Newton* spectra from these pairs of observations using ADDASCASPEC to provide the highest S/N data possible for these two flux regimes. These spectra are shown in Fig. 5.

We initially begin by fitting the high-flux data with a simple absorbed power-law model. We use XSPEC for our spectral analysis (Arnaud 1996), and allow for both the Galactic absorption column of $N_{\rm H,Gal} = 2.33 \times 10^{20}$ cm^{-2} (HI4PI Collaboration 2016) and further absorption at the redshift of NGC 3044 ($z = 0.004\,30$) that is free to vary in all our models. Both absorbers are modelled using TBABS, and we adopt solar abundances from Wilms, Allen & McCray (2000) and absorption cross-sections from Verner et al. (1996). We also allow for cross-normalization constants to float between the data from the pn and MOS detectors to account for residual calibration differences; these factors are always within a few per cent of unity. Finally, the higher flux data are grouped to a minimum of 25 counts per bin to facilitate the use of χ^2 minimization. The absorbed power-law model returns a fairly steep continuum, with $N_{\rm H,high} = (2.1 \pm 0.2) \times 10^{21}$ cm^{-2} and $\Gamma_{\rm high} = 2.41 \pm 0.07$ (uncertainties on the spectral parameters are quoted at the 90 per cent level). Unsurprisingly, the lower flux data have a much lower S/N (in addition to the lower flux, these data have a much lower combined exposure). We therefore group these data to just 1 count per bin, and fit them with the same model using the Cash statistic (Cash 1979). Here we find $N_{\rm H,low} = 1.1^{+0.8}_{-0.7} \times 10^{21}$ cm^{-2} and $\Gamma_{\rm low} = 2.3 \pm 0.4$. Within the limitations of the available data, there is therefore little evidence

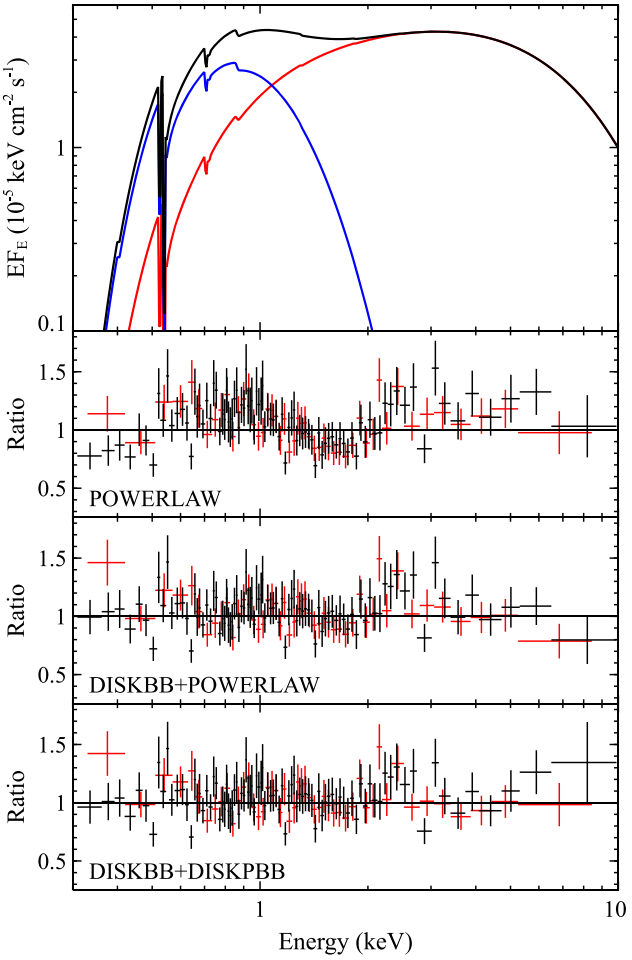

Figure 6. *Top panel:* The relative contributions of the best-fitting DISKBB + DISKPBB model to the high-flux *XMM–Newton* data for NGC 3044 ULX1. The total model is shown in black, the DISKBB component in blue, and the DISKPBB component in red, respectively. *Lower panels:* The data/model ratio for a simple absorbed power-law continuum model, a DISKBB + POWERLAW continuum and the DISKBB + DISKPBB models, respectively. For the ratio panels, the colours have the same meanings as in Fig. 5, and the data have again been rebinned for visual purposes.

for spectral variability, although the parameter constraints are not particularly tight for the lower flux data.

Although the absorbed power-law model captures the overall shape of the spectrum in the 0.3–10.0 keV band fairly well, the high-flux data have sufficient S/N that systematic residuals to this simple model can be seen (see Fig. 6), implying that a more complex continuum model is required. Indeed, the quality of fit provided by the absorbed power-law model for the high-flux data is $\chi^2 = 353$ for 285 degrees of freedom (DoF), which is not formally an acceptable fit. This residual structure is fairly typical for extreme ULXs when fit with a single power-law model (e.g. Stobbart et al. 2006; Gladstone et al. 2009; Mukherjee et al. 2015), and indicates the need for distinct continuum components above and below ∼1–2 keV. We therefore fit the high-flux data with a few more complex models often used to describe ULX spectra. First, we fit a model consisting of a lower energy accretion disc component, and a higher energy power-law continuum. We use the DISKBB model (Mitsuda et al. 1984) for the former, which implicitly assumes a thin-disc profile (Shakura & Sunyaev 1973), such that the model broadly represents the classic

Table 5. Key parameters obtained for the various continuum model fits to the high-flux data available for NGC 3044 ULX1.

Model Component	Parameter	Continuum model		
		POWERLAW	DISKBB + POWERLAW	DISKBB + DISKPBB
TBABS	$N_{\rm H}$ (10^{21} cm^{-2})	2.1 ± 0.2	$3.5^{+0.7}_{-0.6}$	3.0 ± 0.6
DISKBB	$T_{\rm in}$ (keV)	–	0.16 ± 0.02	0.19 ± 0.03
	Norm	–	37^{+80}_{-25}	13^{+26}_{-7}
POWERLAW	Γ	2.41 ± 0.07	2.2 ± 0.1	–
	Norm (10^{-5})	6.1 ± 0.3	$5.0^{+0.6}_{-0.5}$	–
DISKPBB	$T_{\rm in}$ (keV)	–	–	$1.7^{+0.7}_{-0.4}$
	p	–	–	$0.56^{+0.15}_{-0.05}$
	Norm (10^{-4})	–	–	$3.6^{+5.7}_{-0.5}$
χ^2/DoF		353/285	284/283	273/282

disc–corona geometry seen in sub-Eddington X-ray binaries. This provides a significant improvement to the simpler power-law fit, with χ^2/DoF = 284/283. The best-fitting parameters are given in Table 5.

There is still a mild hint of curvature in the spectrum at higher energies though ($E > 2$ keV; Fig. 6). This is seen in the majority of high S/N ULX spectra, initially implied by *XMM–Newton* (e.g. Gladstone et al. 2009; Walton et al. 2011a) and then unambiguously confirmed by the higher energy coverage provided by *NuSTAR* (e.g. Bachetti et al. 2013; Walton et al. 2014; Rana et al. 2015). These broad-band observations find that ULX spectra are primarily described by two thermal components below 10 keV. We therefore also fit a second model that is often considered for ULXs, combining two accretion disc components.[3] Specifically, for the higher energy emission we replace the power-law component with a DISKPBB model (Mineshige et al. 1994). This allows for the radial temperature index (p) to be an additional free parameter, such that the model can mimic a thick, advection-dominated super-Eddington accretion disc (which would be expected to have $p < 0.75$ instead of the $p = 0.75$ appropriate for thin accretion discs; Abramowicz et al. 1988). The DISKBB + DISKPBB does provide a moderate additional improvement in fit over the DISKBB and power-law combination, with χ^2/DoF = 273/282 (i.e. an improvement of $\Delta\chi^2 = 11$ for one extra free parameter). As our best-fitting model, we show the relative contributions of the different model components in Fig. 6, and the parameter constraints are also given in Table 5.

The best-fitting spectral form for NGC 3044 ULX1 differs somewhat from that used to compute the fluxes in 4XMM-DR10, so we also re-calculate the observed 0.3–10 keV fluxes for the individual *XMM–Newton* observations using the spectral models for the high- and low-flux states discussed above. To further examine the long-term behaviour of the source we also consider the *Swift* data at this stage. These observations can themselves be split into two main groups, taken in 2015 April and June. We process the combined data from these two sets of observations, compute the average count rates for each of the two groups using the same 20 arcsec regions as for the *XMM–Newton* data (correcting appropriately for the point spread function), and convert these to fluxes using the spectral shape implied by the simple power-law fits to the *XMM–Newton* data. The long-term light curve combining the *XMM–Newton* and *Swift* data is shown in Fig. 7. The coverage is admittedly sparse, but the *Swift* fluxes are consistent with the more recent *XMM–Newton* measurements, and so it appears as though the higher flux state persisted throughout 2013–2016. We also still find the peak luminosity of the source to be $L_{\rm X,peak} \sim 10^{40}$ erg s^{-1}, confirming the extreme luminosity implied by our analysis of 4XMM-DR10.

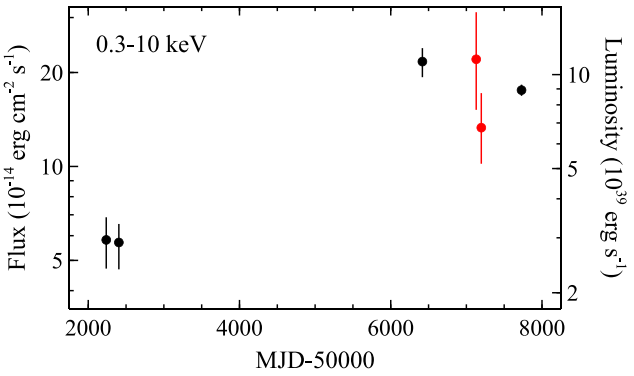

Figure 7. Longtime light curve for NGC 3044 ULX1 based on the available X-ray data. *XMM–Newton* data are shown in black, and *Swift* in red. Note that the sets of *Swift* observations taken in April and in June have been combined together here (see Section 5.2).

5.3 Timing analysis

The longest of the available *XMM–Newton* observations of NGC 3044 ULX1, OBSID 0782650101, returns a total of ∼5000 net source counts with the EPIC-pn detector, roughly comparable to the quality of data used to detect X-ray pulsations for some of the known ULX pulsars (e.g. Israel et al. 2017a; Rodríguez Castillo et al. 2020). We therefore also perform a search for pulsations on this data set. We focus on the data from the EPIC-pn detector here as this has both the highest count rate and the best timing resolution of the EPIC detectors (73.4 ms in the full-frame mode used for this observation).

For this analysis, we use the pulsar timing tools included in the HENDRICS package (Bachetti 2018). Since the pulse period can evolve rapidly in ULX pulsars, either due to the secular spin-up driven by the extreme accretion (Fürst et al. 2016; Israel et al. 2017a; Carpano et al. 2018; Vasilopoulos et al. 2018) or orbital motion of the neutron star (Bachetti et al. 2014; Israel et al. 2017a; Fürst et al. 2018, 2021), we perform an 'accelerated' pulsation search, which considers both

[3]The best *NuSTAR* data available for ULXs show that a third continuum component is typically required above ∼10 keV to model the broad-band spectra (e.g. Walton et al. 2018b). However, without coverage of these energies we cannot say anything about the presence of this component here, and so restrict ourselves to a simpler two-component model for the data below 10 keV.

the frequency of the pulsations (f) and its first derivative ($\dot{f}$) when searching for any signals. Specifically, we use the HENZSEARCH script, which performs the Z_n^2 search originally outlined in Buccheri et al. (1983), and allow for $n = 2$ harmonics in our search (i.e. we use the Z_2^2 statistic). Based on the properties of the known ULX pulsars, we focus on the frequency range of 0.01–6.75 Hz, and the 'fast' search option utilized allows for $\dot{f}$ values in the range $\pm 10^{-8}$ Hz s^{-1}. Unfortunately we did not find any promising pulsation candidates in this observation.

In the absence of a robust pulsation detection, we estimate an upper limit on the pulsed fraction any undetected signal could have following the method used in Walton et al. (2021). In short, we use the HENZN2VSPF script, which simulates data sets using the same GTIs and total number of events as the real data, then uses rejection sampling to modulate the events with an increasingly strong pulsed signal (assuming a sinusoidal pulse profile, which is appropriate for ULX pulsars), and finally calculates the Z_2^2 for each pulsed fraction to see how strongly such pulsations would have been detected. We simulate 100 data sets in order to determine the pulsed fraction at which the Z_2^2 statistic reaches ∼40. This threshold roughly corresponds to a 3σ detection, and thus indicates the equivalent upper limit on the pulsed fraction that could still be present in the real data. We find an upper limit on the pulsed fraction of ∼22 per cent when considering the full *XMM–Newton* bandpass.

5.4 The nature of NGC 3044 ULX1

NGC 3044 ULX1 is a new extreme ULX discovered in our analysis that already has high S/N data available in the archive. Although it has always been in the ULX regime whenever observed with our current X-ray facilities (considering *XMM–Newton* and *Swift* in combination, we have observations from 6 different epochs), sometime between 2002 and 2013 it seemed to jump up by a factor of ∼3–4 in luminosity from $L_{\rm X} \sim 3 \times 10^{39}$ erg s^{-1} to $L_{\rm X} \sim 10^{40}$ erg s^{-1}, where it seems to have remained since (see Fig. 7).

The 0.3–10.0 keV X-ray spectrum observed during this high-flux period is very similar to other extreme ULXs: the flux below 10 keV is dominated by two continuum components that primarily contribute above and below ∼1–2 keV and, although it is not a strong statistical detection, there is a hint of spectral curvature in the higher energy component. We note in particular that, although there is no higher energy coverage available here, the spectrum of NGC 3044 ULX1 is highly reminiscent of that seen from Holmberg II X-1 – another extreme ULX with $L_{\rm X,peak} \sim 10^{40}$ erg s^{-1} – during the broad-band observations performed with *XMM–Newton*, *Suzaku*, and *NuSTAR* in 2013 (Walton et al. 2015). As noted previously, this was part of a series of broad-band observations of ULXs (e.g. Bachetti et al. 2013; Walton et al. 2014; Mukherjee et al. 2015; Rana et al. 2015) that robustly confirmed earlier indications from *XMM–Newton* (e.g. Stobbart et al. 2006; Gladstone et al. 2009; Walton et al. 2011a) that the high-energy spectra of ULXs are distinct from those seen from sub-Eddington black holes. While the spectra from these systems are typically dominated by Comptonization in an optically thin 'corona' above ∼2 keV (e.g. Haardt & Maraschi 1991), the spectra of ULXs instead seem to be dominated by two thermal components below 10 keV, before falling away steeply at higher energies. Indeed, the best-fitting model for the high-flux *XMM–Newton* spectra from NGC 3044 ULX1 consists of two thermal accretion disc components.

The distinct broad-band spectra of ULXs, along with the detection of X-ray pulsations (Bachetti et al. 2014; Fürst et al. 2016; Israel et al. 2017a,b; Carpano et al. 2018; Sathyaprakash et al. 2019; Rodríguez Castillo et al. 2020) and extreme outflows (Pinto et al. 2016, 2017, 2020; Walton et al. 2016; Kosec et al. 2018b) from a growing number of these systems have, together, helped clearly establish that the majority of the ULX population is dominated by super-Eddington accretors. In this context, the two continuum components seen in ULXs below 10 keV likely represent the complex thermal emission from a hot, super-Eddington accretion disc (and potentially its associated outflow; e.g. Poutanen et al. 2007; Middleton et al. 2015). Given its similarity to other, better studied ULXs that are now well accepted to be super-Eddington accretors, NGC 3044 ULX1 is therefore likely another super-Eddington system. As discussed above, these sources are of particular interest, as they may provide a local observational window into the conditions required to rapidly grow SMBHs in the early Universe (e.g. Bañados et al. 2018).

We have searched for X-ray pulsations from NGC 3044 ULX1, which would unambiguously identify the accretor as another neutron star and confirm its nature as a highly super-Eddington system. We focused on the 2016 data, which by far have the best S/N among the available observations, and searched for pulsations over the 0.01–6.75 Hz frequency range based on the properties of the known ULX pulsars, but unfortunately we did not find a robust detection of any such variations. However, even though the available data has quite high S/N, we can only place an upper limit of ∼20 per cent on the pulsed fraction of any pulsations present during this observation. Although pulsations of the strength seen in NGC 300 ULX1 can therefore be firmly excluded (pulsed fraction of ∼60 per cent below 10 keV; Carpano et al. 2018), other known ULX pulsars exhibit pulsed fractions that are lower than this limit in the *XMM–Newton* bandpass (e.g. Sathyaprakash et al. 2019; Rodríguez Castillo et al. 2020). Furthermore, even in ULXs that are known to be pulsars the pulsations can be transient, and are not always observed even when the data should have sufficient S/N to see them (e.g. Israel et al. 2017a; Bachetti et al. 2020). As such, even though we have not seen any clear evidence for X-ray pulsations from NGC 3044 ULX1, we cannot exclude the possibility that this is another neutron star ULX.

Although the comparison with other ULXs is quite compelling, obtaining higher energy data would be of particular use in order to more robustly confirm NGC 3044 ULX1 as another super-Eddington accretor. In the known ULX pulsars, the pulsed fraction is seen to increase with energy, perhaps because non-pulsed components from the accretion flow make a more significant contribution below ∼10 keV (e.g. Walton et al. 2018b). Higher energy coverage would therefore help to mitigate against these issues in terms of further pulsation searches, and would also allow us to extend the continuum spectroscopy above 10 keV, and further confirm that the broad-band spectrum of NGC 3044 ULX1 is similar to other ULXs. Unfortunately, given both the fairly low peak flux from NGC 3044 ULX1 (∼2×10^{-13} erg cm^{-2} s^{-1} in the 0.3–10 keV band; see Fig. 7) and the fairly close proximity of SN1983E (see Fig. 4), meaningful observations of NGC 3044 ULX1 with *NuSTAR* would likely be very challenging. This may, instead, be a suitable target for a facility like the *High-Energy X-ray Probe* (*HEX-P*; Madsen et al. 2018), which would have both superior sensitivity and imaging capabilities to *NuSTAR*.

6 SUMMARY AND OUTLOOK

We have compiled a new catalogue of ULX candidates, combining the latest data releases from each of the *XMM–Newton*, *Swift*, and *Chandra* observatories (the 4XMM-DR10, 2SXPS, and CSC2 source catalogues, respectively). Our new catalogue contains 1843 sources residing in 951 different host galaxies, making it the largest ULX

catalogue compiled to date. Of these, 689 sources are catalogued as ULX candidates for the first time. Our sample also contains 72 HLX candidates, of which 48 are new catalogue entries. We have made significant efforts to clean the catalogue of known non-ULX contaminants (e.g. foreground stars, background AGNs, supernovae), and estimate that the remaining contribution of unknown contaminants is ∼20 per cent. Our primary motivation here is to unearth new sources of interest for detailed follow-up studies, and among this new catalogue we have already found one new extreme ULX candidate with high S/N data in the archive: NGC 3044 ULX1. This shows a factor of at least ∼4 variability on long time-scales, based on the available *XMM–Newton* and *Swift* data, with a peak luminosity of $L_{\rm X,peak} \sim 10^{40}$ erg s^{-1} to date. The *XMM–Newton* spectrum of the source while at this peak flux is reminiscent of other extreme ULXs (and Holmberg II X-1 in particular), and is best-fitting by a model combining two thermal accretion disc components. This likely indicates that NGC 3044 ULX1 is another member of the ULX population accreting at super-Eddington rates.

We anticipate this new catalogue will be a valuable resource for planning further observational campaigns, both with our current X-ray imaging facilities (*XMM–Newton*, *Chandra*, *Swift*, and *NuSTAR*) and with upcoming missions such as *XRISM* and, in particular, *Athena*. Our new catalogue should also help to facilitate further studies of ULXs at longer wavelengths, particularly in the era of the new optical, NIR and radio facilities due to come online (the thirty-metre class ground-based observatories, *JWST*, the SKA). Such work will be vital for determining the contribution of ULX pulsars to the broader ULX population, their accretion physics, the prevalence of extreme outflows among the ULX population and the impact of the winds launched by super-Eddington accretors, and for the hunt for the first dynamically confirmed black hole ULX. Further iterations of the *XMM–Newton*, *Swift*, and *Chandra* serendipitous surveys, combined with the upcoming results from *eROSITA* (Predehl et al. 2021), will also allow us to continue expanding this ULX sample in the future.

ACKNOWLEDGEMENTS

The authors would like to thank the referee for taking the time to review our work. DJW acknowledges support from the Science and Technology Facilities Council (STFC) via an Ernest Rutherford Fellowship (ST/N004027/1). TPR also acknowledges support from STFC via consolidated grant ST/000244/1. SM acknowledges financial support from the Spanish Ministry MCIU under project RTI2018-096686-B-C21 (MCIU/AEI/FEDER/UE), cofunded by FEDER funds and from the Agencia Estatal de Investigación, Unidad de Excelencia Marìa de Maeztu, ref. MDM-2017-0765. This research has made use of data obtained with *XMM–Newton*, an ESA science mission with instruments and contributions directly funded by ESA Member States, as well as public data from the *Swift* data archive. This work has also made use of data obtained from the *Chandra* Source Catalogue, provided by the *Chandra* X-ray Center (CXC) as part of the *Chandra* Data Archive, as well as public data from the Swift data archive. This paper made use of the Whole Sky Database (WSDB) created by Sergey Koposov and maintained at the Institute of Astronomy, Cambridge by Sergey Koposov, Vasily Belokurov, and Wyn Evans with financial support from STFC and the European Research Council (ERC), as well as the Q3C software (Koposov & Bartunov 2006). This research has also made use of the NASA/IPAC Extragalactic Database (NED), which is funded by the National Aeronautics and Space Administration and operated by the California Institute of Technology, as well as the SIMBAD database, operated at CDS, Strasbourg, France, and we further acknowledge usage of the HyperLEDA data base.

DATA AVAILABILITY

All of the raw data underlying this article are publicly available from ESA's *XMM–Newton* Science Archive,[4] NASA's HEASARC data base[5] and NASA's *Chandra* Data Archive.[6] The primary X-ray catalogues (4XMM,[7] 2SXPS,[8] and CSC2[9]), galaxy catalogues (HyperLEDA,[10] CNG,[11] and Cosmicflows[12]), and general catalogues (NED[13] and SIMBAD[14]) used in this work are also all publicly available via the links provided. The final catalogues of ULX candidates produced here will also be made publicly available via the VizieR archive[15] after the publication of this work.

REFERENCES

Abbott R. et al., 2020, Phys. Rev. Lett., 125, 101102
Abramowicz M. A., Czerny B., Lasota J. P., Szuszkiewicz E., 1988, ApJ, 332, 646
Arnaud K. A., 1996, in Jacoby G. H., Barnes J., eds, ASP Conf. Ser. Vol. 101, Astronomical Data Analysis Software and Systems V. Astron. Soc. Pac., San Francisco, p. 17
Arnett W. D., 1982, ApJ, 254, 1
Bachetti M., 2018, Astrophysics Source Code Library, record ascl:1805.019
Bachetti M. et al., 2013, ApJ, 778, 163
Bachetti M. et al., 2014, Nature, 514, 202
Bachetti M. et al., 2020, ApJ, 891, 44
Bañados E. et al., 2018, Nature, 553, 473
Barrows R. S., Mezcua M., Comerford J. M., 2019, ApJ, 882, 181
Brightman M., Walton D. J., Xu Y., Earnshaw H. P., Harrison F. A., Stern D., Barret D., 2020a, ApJ, 889, 71
Brightman M. et al., 2020b, ApJ, 895, 127
Buccheri R. et al., 1983, A&A, 128, 245
Burrows D. N. et al., 2005, Space Sci. Rev., 120, 165
Cappelluti N. et al., 2009, A&A, 497, 635
Carpano S., Haberl F., Maitra C., Vasilopoulos G., 2018, MNRAS, 476, L45
Carrera F. J. et al., 2007, A&A, 469, 27
Cash W., 1979, ApJ, 228, 939
Colbert E. J. M., Mushotzky R. F., 1999, ApJ, 519, 89
Colbert E. J. M., Ptak A. F., 2002, ApJS, 143, 25
Dadina M., Masetti N., Cappi M., Malaguti G., Miniutti G., Ponti G., Gandhi P., De Marco B., 2013, A&A, 559, A86
Dall'Osso S., Perna R., Stella L., 2015, MNRAS, 449, 2144
Earnshaw H. P., Roberts T. P., Sathyaprakash R., 2018, MNRAS, 476, 4272
Earnshaw H. P. et al., 2019a, ApJ, 881, 38
Earnshaw H. P., Roberts T. P., Middleton M. J., Walton D. J., Mateos S., 2019b, MNRAS, 483, 5554
Earnshaw H. P. et al., 2020, ApJ, 891, 153
Eskridge P. B. et al., 2002, ApJS, 143, 73
Evans P. A. et al., 2009, MNRAS, 397, 1177

[4] https://www.cosmos.esa.int/web/xmm-newton/xsa
[5] https://heasarc.gsfc.nasa.gov/
[6] https://cxc.harvard.edu/cda/
[7] http://xmmssc.irap.omp.eu/Catalogue/4XMM-DR10/4XMM_DR10.html
[8] https://www.swift.ac.uk/2SXPS/
[9] https://cxc.harvard.edu/csc/
[10] http://leda.univ-lyon1.fr/
[11] https://www.sao.ru/lv/lvgdb/
[12] http://edd.ifa.hawaii.edu/
[13] https://ned.ipac.caltech.edu/
[14] http://simbad.u-strasbg.fr/simbad/
[15] https://vizier.u-strasbg.fr/viz-bin/VizieR

Evans I. N. et al., 2020a, in American Astronomical Society Meeting Abstracts. Vol. 235, p. 154.05
Evans P. A. et al., 2020b, ApJS, 247, 54
Farrell S. A., Webb N. A., Barret D., Godet O., Rodrigues J. M., 2009, Nature, 460, 73
Feng H., Kaaret P., 2010, ApJ, 712, L169
Fürst F. et al., 2016, ApJ, 831, L14
Fürst F., Walton D. J., Stern D., Bachetti M., Barret D., Brightman M., Harrison F. A., Rana V., 2017, ApJ, 834, 77
Fürst F. et al., 2018, A&A, 616, A186
Fürst F. et al., 2021, A&A, 651, A75
Garmire G. P., Bautz M. W., Ford P. G., Nousek J. A., Ricker G. R. Jr, 2003, in Truemper J. E., Tananbaum H. D., eds, Proc. SPIE Conf. Ser. Vol. 4851, X-Ray and Gamma-Ray Telescopes and Instruments for Astronomy. SPIE, Bellingham, p. 28
Gehrels N., 1986, ApJ, 303, 336
Gehrels N. et al., 2004, ApJ, 611, 1005
Ghosh H., Mathur S., Fiore F., Ferrarese L., 2008, ApJ, 687, 216
Gladstone J. C., Roberts T. P., Done C., 2009, MNRAS, 397, 1836
Gong H., Liu J., Maccarone T., 2016, ApJS, 222, 12
Griffiths R. E., Ptak A., Feigelson E. D., Garmire G., Townsley L., Brandt W. N., Sambruna R., Bregman J. N., 2000, Science, 290, 1325
Guillochon J., Parrent J., Kelley L. Z., Margutti R., 2017, ApJ, 835, 64
Guo J.-C., Liu J.-F., Wang S., Wu Y., Qin Y.-X., 2016, Res. Astron. Astrophys., 16, 34
Haardt F., Maraschi L., 1991, ApJ, 380, L51
Hardcastle M. J. et al., 2007, ApJ, 670, L81
Harrison F. A. et al., 2013, ApJ, 770, 103
Heida M., Jonker P. G., Torres M. A. P., Roberts T. P., Miniutti G., Fabian A. C., Ratti E. M., 2013, MNRAS, 433, 681
Heida M. et al., 2019, ApJ, 883, L34
HI4PI Collaboration, 2016, A&A, 594, A116
Høg E. et al., 2000, A&A, 355, L27
Inoue Y., Tanaka Y. T., Isobe N., 2016, MNRAS, 461, 4329
Inoue Y., Yabe K., Ueda Y., 2021, preprint (arXiv:2107.07775)
Israel G. L. et al., 2017a, Science, 355, 817
Israel G. L. et al., 2017b, MNRAS, 466, L48
Jansen F. et al., 2001, A&A, 365, L1
Kaaret P., Feng H., Roberts T. P., 2017, ARA&A, 55, 303
Karachentsev I. D., Kaisina E. I., Makarov D. I., 2018, MNRAS, 479, 4136
King A. R., Davies M. B., Ward M. J., Fabbiano G., Elvis M., 2001, ApJ, 552, L109
Koliopanos F., Vasilopoulos G., Godet O., Bachetti M., Webb N. A., Barret D., 2017, A&A, 608, A47
Koposov S., Bartunov O., 2006, in Gabriel C., Arviset C., Ponz D., Enrique S., eds, ASP Conf. Ser. Vol. 351, Astronomical Data Analysis Software and Systems XV. Astron. Soc. Pac., San Francisco, p. 735
Kosec P., Pinto C., Fabian A. C., Walton D. J., 2018a, MNRAS, 473, 5680
Kosec P., Pinto C., Walton D. J., Fabian A. C., Bachetti M., Brightman M., Fürst F., Grefenstette B. W, 2018b, MNRAS, 479, 3978
Kovlakas K., Zezas A., Andrews J. J., Basu-Zych A., Fragos T., Hornschemeier A., Lehmer B., Ptak A., 2020, MNRAS, 498, 4790
Lehmer B. D. et al., 2019, ApJS, 243, 3
Liu J., 2011, ApJS, 192, 10
Liu J., Bregman J. N., 2005, ApJS, 157, 59
Liu Q. Z., Mirabel I. F., 2005, A&A, 429, 1125
Lopez L. A., Mathur S., Nguyen D. D., Thompson T. A., Olivier G. M., 2020, ApJ, 904, 152
Madsen K. K. et al., 2018, Proc. SPIE Conf. Ser. Vol. 10699, Space Telescopes and Instrumentation 2018: Ultraviolet to Gamma Ray. SPIE, Bellingham, p. 106996M
Makarov D., Prugniel P., Terekhova N., Courtois H., Vauglin I., 2014, A&A, 570, A13
Masini A. et al., 2020, ApJS, 251, 2
Mateos S. et al., 2008, A&A, 492, 51
Mezcua M., Roberts T. P., Lobanov A. P., Sutton A. D., 2015, MNRAS, 448, 1893
Middleton M. J., Sutton A. D., Roberts T. P., Jackson F. E., Done C., 2012, MNRAS, 420, 2969
Middleton M. J. et al., 2013, Nature, 493, 187
Middleton M. J., Heil L., Pintore F., Walton D. J., Roberts T. P., 2015, MNRAS, 447, 3243
Miller J. M. et al., 2004, ApJ, 601, 450
Mineo S., Gilfanov M., Sunyaev R., 2012, MNRAS, 419, 2095
Mineo S., Rappaport S., Steinhorn B., Levine A., Gilfanov M., Pooley D., 2013, ApJ, 771, 133
Mineshige S., Hirano A., Kitamoto S., Yamada T. T., Fukue J., 1994, ApJ, 426, 308
Mitsuda K. et al., 1984, PASJ, 36, 741
Mondal S., Belczyński K., Wiktorowicz G., Lasota J.-P., King A. R., 2020, MNRAS, 491, 2747
Mukherjee E. S. et al., 2015, ApJ, 808, 64
Mushtukov A. A., Suleimanov V. F., Tsygankov S. S., Poutanen J., 2015, MNRAS, 454, 2539
Nandra K. et al., 2013, preprint (arXiv:1306.2307)
Pasham D. R., Strohmayer T. E., Mushotzky R. F., 2014, Nature, 513, 74
Piconcelli E., Jimenez-Bailón E., Guainazzi M., Schartel N., Rodríguez-Pascual P. M., Santos-Lleó M., 2004, MNRAS, 351, 161
Pinto C., Middleton M. J., Fabian A. C., 2016, Nature, 533, 64
Pinto C. et al., 2017, MNRAS, 468, 2865
Pinto C. et al., 2020, MNRAS, 492, 4646
Pintore F., Zampieri L., Stella L., Wolter A., Mereghetti S., Israel G. L., 2017, ApJ, 836, 113
Pintore F. et al., 2018, MNRAS, 477, L90
Pintore F. et al., 2020, ApJ, 890, 166
Plucinsky P. P., Bogdan A., Marshall H. L., Tice N. W., 2018, in Proc. SPIE Conf. Ser. Vol. 10699, Space Telescopes and Instrumentation 2018: Ultraviolet to Gamma Ray. SPIE, Bellingham, p. 106996B
Poutanen J., Lipunova G., Fabrika S., Butkevich A. G., Abolmasov P., 2007, MNRAS, 377, 1187
Predehl P. et al., 2021, A&A, 647, A1
Rana V. et al., 2015, ApJ, 799, 121
Roberts T. P., Warwick R. S., 2000, MNRAS, 315, 98
Rodríguez Castillo G. A. et al., 2020, ApJ, 895, 60
Russell D. G., 2002, ApJ, 565, 681
Sathyaprakash R. et al., 2019, MNRAS, 488, L35
Servillat M., Farrell S. A., Lin D., Godet O., Barret D., Webb N. A., 2011, ApJ, 743, 6
Shakura N. I., Sunyaev R. A., 1973, A&A, 24, 337
Shu Y., Koposov S. E., Evans N. W., Belokurov V., McMahon R. G., Auger M. W., Lemon C. A., 2019, MNRAS, 489, 4741
Song X., Walton D. J., Lansbury G. B., Evans P. A., Fabian A. C., Earnshaw H., Roberts T. P., 2020, MNRAS, 491, 1260
Soria R., Kuntz K. D., Winkler P. F., Blair W. P., Long K. S., Plucinsky P. P., Whitmore B. C., 2012, ApJ, 750, 152
Stobbart A.-M., Roberts T. P., Wilms J., 2006, MNRAS, 368, 397
Strohmayer T. E., Mushotzky R. F., 2009, ApJ, 703, 1386
Strüder L. et al., 2001, A&A, 365, L18
Sutton A. D., Roberts T. P., Walton D. J., Gladstone J. C., Scott A. E., 2012, MNRAS, 423, 1154
Sutton A. D., Roberts T. P., Gladstone J. C., Walton D. J., 2015, MNRAS, 450, 787
Swartz D. A., Ghosh K. K., Tennant A. F., Wu K., 2004, ApJS, 154, 519
Swartz D. A., Tennant A. F., Soria R., 2009, ApJ, 703, 159
Swartz D. A., Soria R., Tennant A. F., Yukita M., 2011, ApJ, 741, 49
Theureau G., Hanski M. O., Coudreau N., Hallet N., Martin J. M., 2007, A&A, 465, 71
Tsygankov S. S., Mushtukov A. A., Suleimanov V. F., Poutanen J., 2016, MNRAS, 457, 1101
Tully R. B., Courtois H. M., Sorce J. G., 2016, AJ, 152, 50
Turner M. J. L. et al., 2001, A&A, 365, L27
van Haaften L. M., Maccarone T. J., Rhode K. L., Kundu A., Zepf S. E., 2019, MNRAS, 483, 3566
Vasilopoulos G., Haberl F., Carpano S., Maitra C., 2018, A&A, 620, L12

Vasilopoulos G., Petropoulou M., Koliopanos F., Ray P. S., Bailyn C. B., Haberl F., Gendreau K., 2019, MNRAS, 488, 5225
Verner D. A., Ferland G. J., Korista K. T., Yakovlev D. G., 1996, ApJ, 465, 487
Véron-Cetty M. P., Véron P., 2010, A&A, 518, A10
Walton D. J., Gladstone J. C., Roberts T. P., Fabian A. C., Caballero-Garcia M. D., Done C., Middleton M. J., 2011a, MNRAS, 414, 1011
Walton D. J., Roberts T. P., Mateos S., Heard V., 2011b, MNRAS, 416, 1844
Walton D. J. et al., 2013, ApJ, 779, 148
Walton D. J. et al., 2014, ApJ, 793, 21
Walton D. J. et al., 2015, ApJ, 806, 65
Walton D. J. et al., 2016, ApJ, 826, L26
Walton D. J. et al., 2018a, ApJ, 857, L3
Walton D. J. et al., 2018b, ApJ, 856, 128
Walton D. J. et al., 2021, MNRAS, 501, 1002
Wang S., Qiu Y., Liu J., Bregman J. N., 2016, ApJ, 829, 20
Webb N. et al., 2012, Science, 337, 554
Webb N. A. et al., 2020, A&A, 641, A136
Weisskopf M. C., Brinkman B., Canizares C., Garmire G., Murray S., Van Speybroeck L. P., 2002, PASP, 114, 1
Wilms J., Allen A., McCray R., 2000, ApJ, 542, 914
XRISM Science Team, 2020, preprint (arXiv:2003.04962)
Zhang W. M., Soria R., Zhang S. N., Swartz D. A., Liu J. F., 2009, ApJ, 699, 281
Zombeck M. V., Chappell J. H., Kenter A. T., Moore R. W., Murray S. S., Fraser G. W., Serio S., 1995, in Siegmund O. H., Vallerga J. V., eds, Proc. SPIE Conf. Ser. Vol. 2518, EUV, X-Ray, and Gamma-Ray Instrumentation for Astronomy VI. SPIE, Bellingham, p. 96

This paper has been typeset from a TEX/LATEX file prepared by the author.